

Optimal experimental design with k-space data: application to inverse hemodynamics

Miriam Lücke Ahmed Attia Dariusz Uciński Cristóbal Bertoglio

December 9, 2025

Abstract

Subject-specific cardiovascular models rely on parameter estimation using measurements such as 4D Flow MRI data. However, acquiring high-resolution, high-fidelity functional flow data is costly and taxing for the patient. As a result, there is growing interest in using highly undersampled MRI data to reduce acquisition time and thus the cost, while maximizing the information gain from the data. Examples of such recent work include inverse problems to estimate boundary conditions of aortic blood flow from highly undersampled k-space data. The undersampled data is selected based on a predefined sampling mask which can significantly influence the performance and the quality of the solution of the inverse problem. While there are many established sampling patterns to collect undersampled data, it remains unclear how to select the best sampling pattern for a given set of inference parameters. In this paper we propose an Optimal Experimental Design (OED) framework for MRI measurements in k-space, aiming to find optimal masks for estimating specific parameters directly from k-space. As OED is typically applied to sensor placement problems in spatial locations, this is, to our knowledge, the first time the technique is used in this context. We demonstrate that the masks optimized by employing OED consistently outperform conventional sampling patterns in terms of parameter estimation accuracy and variance, facilitating a speed-up of 10x of the acquisition time while maintaining accuracy.

1 Introduction

The personalization of hemodynamic models is a key aspect in achieving patient-specific predictions in medical treatments. This requires high-quality clinical data for the formulation and the numerical solution of inverse problems. Using blood velocity measurements from Phase-Contrast Magnetic Resonance Imaging (PC-MRI) is an appealing choice because it is both non-invasive and non-ionizing. The acquisition time of 4D Flow MRI for a high-resolution image, however, can be very high which can be taxing for both patients and medical providers [1, 2].

As a result, it has become common practice to reduce the acquisition time by acquiring only part of the frequency space (also called k-space) that MR images are measured in. These undersampled measurements are then reconstructed by using Compressed Sensing (CS) techniques [3, 4]. Because MRI enables acquiring single lines of the k-space, it provides a wide variety of possible undersampling patterns. Different CS algorithms take advantage of the qualities of these patterns to construct accurate images [5]. For example, pseudo-random sampling patterns contain artifacts of an incoherent nature, which can be removed by assuming sparsity of the true image in other domains. Other CS algorithms leverage the mathematical properties of other common designs such as spirals or radial patterns [6, 7], while others rely on broader properties of the signal such as relative consistency in time or space [8].

Nonetheless, the reconstructed velocity images contain artifacts which negatively impact the results of the solution of the inverse problem. Therefore, we have recently proposed to solve the inverse problem directly from the undersampled frequency space measurements [9]. This approach was exemplified via a Kalman filter adapted specifically for highly undersampled k-space data to estimate boundary condition parameters of the underlying blood flow model given by the incompressible Navier-Stokes equations.

This approach does not consider how the choice of sampling pattern depends on the measurements and how it may affect the outcome of the inverse problem. Instead, there is a plethora of possible design choices with barely even heuristics to make a selection. Additionally, it seems reasonable that different boundary conditions or flow parameters may be better estimated by different masks, which has also not been explored.

Optimal Experimental Design (OED)[10–12] aims to find optimal ways to perform an experiment, such as optimal sensor locations, based on statistical criteria. Optimal designs can be used to reduce the costs of an experiment, since a lesser number of measurements are needed to achieve the same precision. Therefore, OED has been successfully used in applications in a large number of different fields.

In this work we develop an OED approach to identify optimal sampling patterns specific to the inference parameters, that is the parameters estimated by the inverse problem. We demonstrate that there are indeed specific frequencies that are more informative for each parameter. Thus the OED-based optimal masks yield lower errors and variances in the estimated parameters with a lower acquisition time due to the reduced number of sampled frequencies.

The rest of the paper is organized as follows. Section 2 explains the definitions of the measurement model, the OED problem, and the inverse problem. Section 3 describes the setup and results of a simplified analytical test case, while Section 4 provides the same for a more complex test case modelling the hemodynamics in a section of the aorta. Finally, we conclude with a discussion of our results in Section 5 and a conclusion in Section 6.

2 Theory

2.1 The forward problem

Given the parameters $\boldsymbol{\theta} \in \mathbb{R}^p$, for example the physical constants of PDE, and a dynamic state $\mathbf{X}^{k-1} \in \mathbb{R}^r$ at time t^{k-1} with a known initial condition \mathbf{X}^0 , we define the forward problem as:

$$\mathbf{X}^k = \mathcal{A}^k(\mathbf{X}^{k-1}, \boldsymbol{\theta}), \quad k > 0, \quad (1)$$

with $\mathcal{A}^k : \mathbb{R}^r \times \mathbb{R}^p \rightarrow \mathbb{R}^r$ mapping a vector of parameters and the state from the time step t^{k-1} to the state at the next time step t^k . Later, we will also use $\mathcal{A}^k(\boldsymbol{\theta})$ to denote the solution of the forward problem at time t^k based on the fixed initial condition rather than a specific previous state, that is

$$\mathbf{X}^k = \mathcal{A}^k \circ \dots \circ \mathcal{A}^1(\mathbf{X}^0, \boldsymbol{\theta}), \quad k > 0, \quad (2)$$

where \circ denotes the composition of operators.

We define the spatial undersampling operator as $\mathcal{H} : \mathbb{R}^r \rightarrow \mathbb{R}^{N_1 \times \dots \times N_D}$ for a number of dimensions D . For example, for a two-dimensional test case $D = 2$, but for a full 3D acquisition of the blood flow with a velocity vector consisting of components for each direction, $D = 4$ (one for each spatial dimension and one for the velocity components). We will call $N = N_1 \dots N_D$ the total number of samples.

Next, we define the k-space observation operator $\mathcal{H}_{\mathcal{F}} : \mathbb{R}^r \rightarrow \mathbb{R}^{N_1 \times \dots \times N_D}$ as:

$$\mathcal{H}_{\mathcal{F}}(\mathbf{X}) = \mathcal{F} \left[\mathbf{M} \odot e^{i \left(\frac{\pi}{v_{enc}} \mathcal{H}(\mathbf{X}) + \phi_0 \right)} \right], \quad (3)$$

where \odot denotes the Hadamard product, \mathbf{X} is the dynamic state, $vinc$ is the velocity encoding parameter, and $\mathcal{F} : \mathbb{C}^{N_1 \times \dots \times N_D} \rightarrow \mathbb{C}^{N_1 \times \dots \times N_D}$ is the D -dimensional discrete Fourier transform defined as

$$\mathcal{F}[\mathbf{V}]_{y_1 \dots y_D} = \sum_{n_1=0}^{N_1-1} \dots \sum_{n_D=0}^{N_D-1} \mathbf{V}_{n_1 \dots n_D} \exp \left(-i2\pi \left(\frac{y_1 n_1}{N_1} + \dots + \frac{y_D n_D}{N_D} \right) \right). \quad (4)$$

The tensor $\phi_0 \in [-\pi, \pi)^{N_1 \times \dots \times N_D}$ denotes the background phase and $\mathbf{M} \in \mathbb{R}^{N_1 \times \dots \times N_D}$ the magnitude of the magnetization. We assume that ϕ_0 , \mathbf{M} , and $vinc$ are all given.

For a *true* parameter θ_{true} , the k-space measurements at time t^k , i.e., $\mathbf{Y}^k \in \mathbb{C}^{N_1 \times \dots \times N_D}$ for $k = 1, \dots, N_T$, are defined as:

$$\mathbf{Y}^k = \left(\mathcal{H}_{\mathcal{F}} \left(\mathcal{A}^k(\theta_{true}) \right) + \epsilon \right) \odot \mathbf{S}, \quad (5)$$

where $\epsilon \in \mathbb{C}^{N_1 \times \dots \times N_D}$ is a complex Gaussian noise with zero mean and standard deviation σ_y . The measurement noise ϵ is assumed to be proper, meaning there are no correlations between the real and the imaginary parts of the signal. The binary tensor $\mathbf{S} \in \mathbb{R}^{N_1 \times \dots \times N_D}$ models the sampling mask with a multi-index $i = (i_1, \dots, i_D)$:

$$\mathbf{S}_i = \begin{cases} 1 & \text{if the frequency } i \text{ is sampled,} \\ 0 & \text{otherwise.} \end{cases} \quad (6)$$

The measurement provided in a *zero-filled* form, with the unavailable measurements replaced by 0 such that the dimension of the undersampled measurement matches the spatial dimension despite the undersampling. A key quantity for determining the scan time in MRI, when comparing the accuracy given by different masks, is the acceleration factor R defined as

$$R = \frac{N}{\sum_i \mathbf{S}_i}, \quad (7)$$

where N is the total number of samples, and $\sum_i \mathbf{S}_i$ is the total number of sampled frequencies.

2.2 The inverse problem

We formulate the parameter estimation problem as it is done in [9] through a data fidelity term in terms of the frequency space, therefore leading to the minimization problem:

$$\hat{\theta} \in \underset{\theta \in \mathbb{R}^p}{\operatorname{argmin}} \frac{1}{2\sigma_y^2} \sum_{k=1}^{N_T} \|\Re(\mathbf{Y}^k - \mathcal{H}_{\mathcal{F}}(\mathcal{A}^k(\theta)) \odot \mathbf{S})\|^2 + \|\Im(\mathbf{Y}^k - \mathcal{H}_{\mathcal{F}}(\mathcal{A}^k(\theta)) \odot \mathbf{S})\|^2 \quad (8)$$

with the norm $\|\mathbf{X}\|^2 = \sum_{i_1, \dots, i_D} |\mathbf{X}_{i_1, \dots, i_D}|^2$. Here $\Re(\cdot)$, $\Im(\cdot)$, refer to the real- and the imaginary components of a complex-valued signal.

In order to optimize the cost function, we are using the Reduced Order Unscented Kalman Filter (ROUKF) to estimate the parameters θ while assuming perfect knowledge of the initial condition. ROUKF requires an initial guess for the parameters. However, we perform some iterations on this by re-starting the ROUKF algorithm using the result of the previous run as the new initial guess, while keeping the standard deviation of the prior distribution unchanged, as was proposed in [13]. The details of the ROUKF algorithm is provided in Appendix B.

This algorithm requires knowledge of the standard deviation σ_y of the error. As this is generally unknown, we instead estimate it by assuming that the signal in the initial condition \mathbf{X}^0 is zero. Then the transformed signal in frequency space at that time step should be $\mathcal{H}_{\mathcal{F}}(\mathbf{X}) = \mathcal{F}[\mathbf{M} \odot e^{i\phi_0}] \odot \mathbf{S}$. The noise can now be isolated by subtracting this quantity from the actual measurement, allowing the estimation of the standard deviation.

2.3 The Optimal Experimental Design problem

2.3.1 Formulation

The goal of the OED problem is to find the mask (the experimental design) \mathbf{S} out of a suitable design region by solving the following optimization problem:

$$\hat{\mathbf{S}} = \underset{\mathbf{S}}{\operatorname{argmin}} \Phi(\mathbf{S}), \quad \text{s.t.} \quad \sum_i \mathbf{S}_i = N_S \leq N, \quad (9)$$

where $\Phi(\mathbf{S})$ is an OED optimality criterion that does not only depend on a given mask \mathbf{S} , but also on the initial guess of the parameters $\boldsymbol{\theta}_0$ used at the first ROUKF run, that is $\Phi(\mathbf{S}) \equiv \Phi(\mathbf{S}, \mathcal{H}_{\mathcal{F}}(\mathcal{A}(\boldsymbol{\theta}_0)))$.

Note that the constraint $\sum_i \mathbf{S}_i = N_S \leq N$ results in a combinatorial problem of picking N_S out of N voxels to construct a discrete design.

2.3.2 Optimality criterion

The most commonly used optimality criteria are based on the Fisher information matrix (FIM) associated with the estimated parameters [11, 14, 15]. Here, we construct the FIM based on the sensitivity coefficients, which are derivatives of the observed output with respect to the unknown parameters:

$$\frac{\partial \tilde{\mathbf{Y}}^k(\boldsymbol{\theta}_0)}{\partial \theta_1}, \dots, \frac{\partial \tilde{\mathbf{Y}}^k(\boldsymbol{\theta}_0)}{\partial \theta_p}, \quad k = 1, \dots, N_T, \quad (10)$$

with

$$\tilde{\mathbf{Y}}^k(\boldsymbol{\theta}_0) = \mathcal{H}_{\mathcal{F}}(\mathcal{A}^k(\boldsymbol{\theta}_0)) \odot \mathbf{S}, \quad (11)$$

and therefore:

$$\frac{\partial \tilde{\mathbf{Y}}^k}{\partial \theta_j} = \mathcal{F} \left[i \frac{\pi}{\text{vec}} \mathbf{M} \odot e^{i(\frac{\pi}{\text{vec}} \mathcal{H}(\mathcal{A}^k(\boldsymbol{\theta})) + \phi_0)} \odot \mathcal{H} \left(\frac{\partial}{\partial \theta_j} \mathcal{A}^k(\boldsymbol{\theta}) \right) \right] \odot \mathbf{S}. \quad (12)$$

The formula (12) still requires the computation of the sensitivities of the forward problem with respect to the parameters, which in this work will be calculated numerically using the finite difference method[11, Chapter 2.6]. To be precise, we approximate $\frac{\partial}{\partial \theta_j} \mathcal{A}^k(\boldsymbol{\theta})$ as

$$\frac{\partial \mathcal{A}^k(\boldsymbol{\theta})}{\partial \theta_j} \approx \frac{\mathcal{A}^k(\tilde{\boldsymbol{\theta}}) - \mathcal{A}^k(\boldsymbol{\theta})}{h \theta_j} \quad (13)$$

where $\tilde{\boldsymbol{\theta}}$ is the disturbed vector of parameters such that $\tilde{\theta}_i = \theta_i$ for $i \neq j$, $\tilde{\theta}_j = (1 + h)\theta_j$.

Finally, the FIM is defined by

$$\mathbf{F} = \sum_{k=1}^{N_T} \sum_{i=1}^N \frac{2}{\sigma_y^2} \Re \left((\mathbf{G}^k)^* (\mathbf{G}^k)^T \right) \in \mathbb{R}^{p \times p} \quad (14)$$

where $*$ is the complex conjugate transpose and \mathbf{G}^k is the matrix of sensitivity coefficients defined as

$$\mathbf{G}^k = \begin{bmatrix} \left(\text{vec} \left(\frac{\partial \tilde{\mathbf{Y}}^k(\boldsymbol{\theta})}{\partial \theta_1} \right) \right)^T \\ \vdots \\ \left(\text{vec} \left(\frac{\partial \tilde{\mathbf{Y}}^k(\boldsymbol{\theta})}{\partial \theta_p} \right) \right)^T \end{bmatrix} \in \mathbb{C}^{p \times N}, \quad (15)$$

with $\text{vec}(\mathbf{A})$ being the vector formed by stacking columns of the matrix \mathbf{A} .

There are several choices available for the design criterion Φ and it is not always clear a priori which criterion leads to the best results. The most common choices, which we will consider later in our numerical experiments, are [12]:

1. **A-criterion:** $\Phi = \text{tr}(\mathbf{F}^{-1})$. This criterion minimizes the trace of the inverse of the FIM, and therefore minimizes the average variance of the parameters.
2. **D-criterion:** $\Phi = \det(\mathbf{F}^{-1})$. This criterion minimizes the volume of the uncertainty ellipsoid of the parameters, thus also maximizing the Shannon information content of the estimated parameters.

2.3.3 Optimization algorithms

We consider two different algorithms to solve the combinatorial optimization problem with binary designs. The first is a greedy method, detailed in Algorithm 1. At each iteration the greedy algorithm chooses the frequency (out of all currently unused frequencies) that minimizes the optimality criterion when added to the mask. The algorithm stops when the specified number of frequencies has been selected. As the FIM may be singular, a very small constant is added to the diagonal values to ensure that inverting the matrix is possible. The greedy algorithm does not guarantee finding the global optimum, but its time complexity is linear in the number of frequencies N_S to select and the total number of voxels N , and therefore it is convenient in practice.

Algorithm 1 Greedy algorithm

- 1: Start with an empty mask $\mathbf{S} = [\mathbf{S}_i = 0]_{i=(i_1, \dots, i_D)}$
 - 2: $j \leftarrow 0$
 - 3: **while** $j < N_S$ **do**
 - 4: Find $k = (n_1, \dots, n_D)$ that minimizes $\Phi(\mathbf{S})$ when setting $\hat{\mathbf{S}}_k = 1$ where $\mathbf{S}_k = 0$
 - 5: Set $\mathbf{S}_k = 1$
 - 6: $j \leftarrow j + 1$
 - 7: **end while**
-

The second algorithm we consider is the exchange method [12], detailed in Algorithm 2. The method starts with a random selection of the specified number of frequencies N_s . At each iteration, the algorithm finds the best exchange between any one of the currently selected frequencies and a neighboring frequency that is not currently part of the design. The neighboring indices are defined as being contained within a sphere of a given radius around the currently examined frequency. For a sufficiently large radius, the algorithm will therefore consider exchanges with all available frequencies. This algorithm terminates if there is no exchange possible that improves the optimality criterion beyond a certain tolerance. The total runtime of the algorithm is not known a priori and also depends on the random seed used to generate the initial mask.

A critical factor influencing the runtime of the exchange algorithm is possibly frequent inversion of the FIM after perturbation of the original FIM. That is why in the analytical case below the Sherman-Morrison-Woodbury formulae have been used. Indeed, it is easy to see that addition/deletion of a frequency to/from the current set of selected frequencies amounts to a rank-2 perturbation of the FIM. This approach, however, cannot be applied to the aortic hemodynamics setting that follows, since the appropriate perturbations have ranks $\min(p, 2N_T)$, i.e., they are by no means small-rank. Therefore, relatively simple exchanges typically used for numerical construction of directly constrained design measures [12, Chapter 4.3], also known

as clusterization-free designs[11, Chapter 3.4](Uciński, 2005, Ch. 3.4) have been adopted. The technique is applicable in the case of a dense grid of frequencies, which is valid here.

Algorithm 2 Restricted exchange algorithm

```

1: Sample  $N_S$  frequencies randomly to create  $\mathbf{S}^0$ 
2:  $k \leftarrow 1$ 
3: while True do
4:   Define the neighborhood  $\mathcal{N}(\mathbf{S}^{k-1}) = \{i \text{ s.t. } \|k - i\| < \text{radius for a } j \in \mathbf{S}^{k-1}, \mathbf{S}_j^{k-1} = 1\}$ 
5:   Find  $(i^k, j^k) \in \mathbf{S}^{k-1} \times (\mathcal{N}(\mathbf{S}^{k-1}) \setminus \mathbf{S}^{k-1})$  that minimizes  $\Psi(\mathbf{S}_{i \rightleftharpoons j}^{k-1})$  where  $\mathbf{S}_{i \rightleftharpoons j}^{k-1}$  switches
     the values of  $\mathbf{S}$  at  $i$  and  $j$ .
6:   if  $\Psi(\mathbf{S}_{i \rightleftharpoons j}^{k-1}) < \Psi(\mathbf{S}^{k-1})$  then
7:     Set  $\mathbf{S}^k = \mathbf{S}_{i \rightleftharpoons j}^{k-1}$  and continue
8:   else
9:     break ▷ stop if there is insufficient improvement
10:  end if
11: end while

```

3 Analytical Test Case

In this section we consider a simple case in which the measurement sensitivities can be computed analytically. Additionally, we construct the signal to have a specific significant frequencies in order to be able to confirm the results of the OED algorithms. First, we therefore describe the forward problem and our measurements, then the computation of the sensitivities, followed by details of the implementation of the algorithms. We then show both the optimal masks and the conventional masks we are using for comparison and their results on the inverse problem. Lastly, we explore the effects of using sensitivities computed with approximated parameters rather than accurate ones.

3.1 Forward and measurement models

To explore the effect of specific frequencies, we use a simple two-dimensional function

$$f(x, y) = c_0 + c_1x + c_2y + c_3 \sin(2\pi\omega x), \quad (16)$$

with $c_0 = 1.0, c_1 = 0.2, c_2 = 0.5, c_3 = 1.0$ which combines a first-order polynomial with a sine function with a frequency $\omega = 7$. The coefficients c_i are the parameters to be estimated, while ω is assumed to be known. We consider this function in the domain $[0, 1]^2$ which is discretized with 32 elements in each direction, which in frequency space results in 16 positive and 15 negative frequencies in each direction. The function is transformed into MRI-like frequency space data as described by (5), by using a constant magnitude of 1, a constant background phase $\phi_0 = 0.0075$ and velocity encoding parameter $venc = 3$. Figure 1 shows images of the original function as well as the frequency space data. In frequency space, despite the MRI-like transform preceding the Fourier transform, the sinusoidal frequency at $\omega = 7$ is clearly visible, as well as the horizontal and vertical “stripes” deriving from the convolution with the linear parts of the function.

3.2 Sensitivities

The sensitivities for each parameter are computed analytically according to (12). Images of the magnitudes of the sensitivities for each parameter are shown in Figure 2. It is apparent

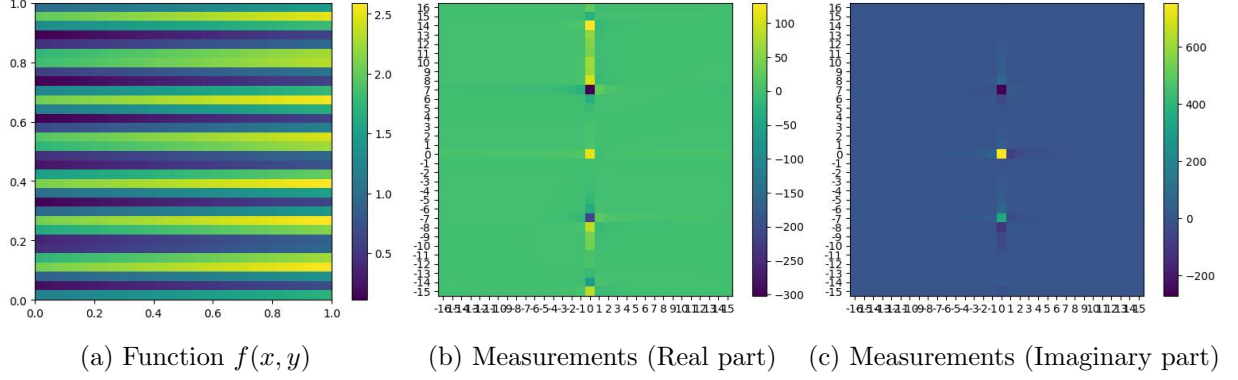


Figure 1: Visualization of the analytical function (16) (a), and the MRI-like measurement signal in frequency space (b) and (c).

that different frequencies are more sensitive to each of the coefficients, depending on their basis function. Notably, as c_0, c_1 and c_2 all relate to polynomials, the highest values of their sensitivity is concentrated around the center frequency $(0, 0)$, while this frequency has a sensitivity close to zero for c_3 , which relates to a sinusoidal function.

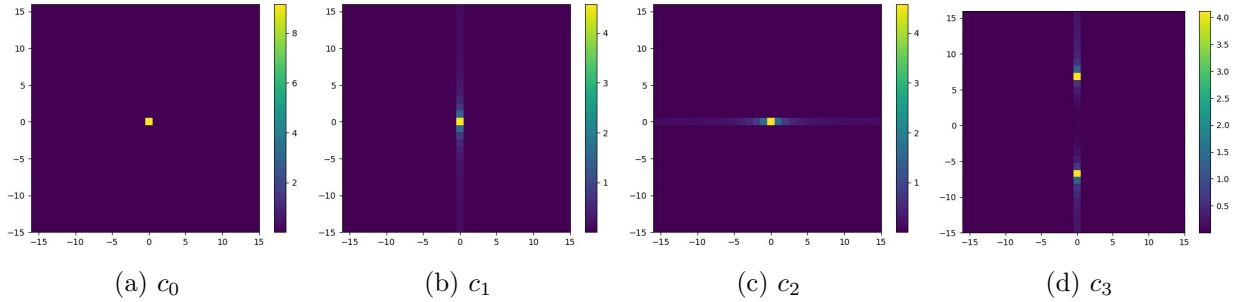


Figure 2: Magnitude of the sensitivities of the measurement for each of the parameters in the analytical test case (16). The parameters here are the constant component c_0 , the linear x-component c_1 , linear y-component c_2 , and the sinusoidal component c_3 , respectively.

3.3 Implementation of the optimization algorithms

For the greedy algorithm, we use the implementation provided by the PyOED package [16]. For the exchange algorithm, we choose to use a radius of 10 voxels and a tolerance of 10^{-8} , as we have found that further increasing the radius or decreasing the tolerance does not change the result of the algorithm. We use our own implementation of this algorithm in Python.

In terms of computational cost, we list the computation times in Table 1, computed on a notebook with 16GB RAM and an Intel Core i5 processor. The greedy algorithm requires a longer computation time than the exchange algorithm for lower budgets, but scales better, leading to a shorter time for a budget of 50 points.

3.4 Optimal masks

We solve the OED problem with both A-optimality and D-optimality criteria, and with masks for four different budgets $N_S = 5, 10, 25, 50$. These budgets correspond to acceleration factor

Algorithm	budget (N_s)			
	5	10	25	50
Greedy	6.5s	12.96s	33.81s	1min 27s
Exchange	0.49s	3.09s	18.23s	1min 6s

Table 1: Compute time (in seconds) for the two algorithms for different budgets on the analytical testcase (16).

values of $R \sim 205, 102, 41, 21$, respectively. The resulting optimal masks for the combinations of optimality criteria, budgets, and optimization algorithms, are shown in Figures 3—7.

For lower budgets, as seen in Figures 3 and 5, the masks are very similar between criteria and algorithms, with frequencies near the center and at the wave frequency mainly being selected.

For higher budgets, as seen in Figures 6 and 7, differences between the algorithms become apparent. While the greedy algorithm tends to select frequencies mainly along the vertical and horizontal axes, the exchange algorithm clusters points around the center and the wave frequency. For both algorithms, the D-criterion results in more points being selected along the vertical axis, whereas the A-criterion leads to the selection of more horizontal points, either on the central axis or as “branches” off points on the central vertical axis.

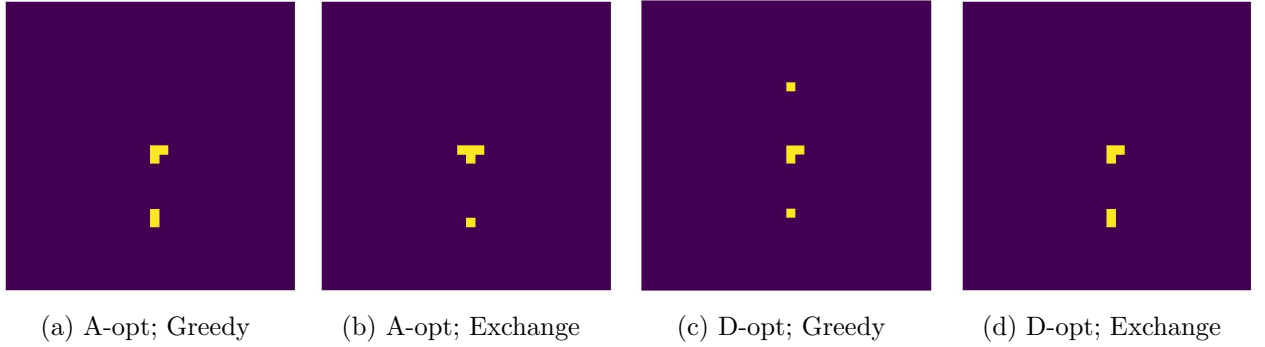


Figure 3: Masks for a budget of $N_S = 5$ frequencies.

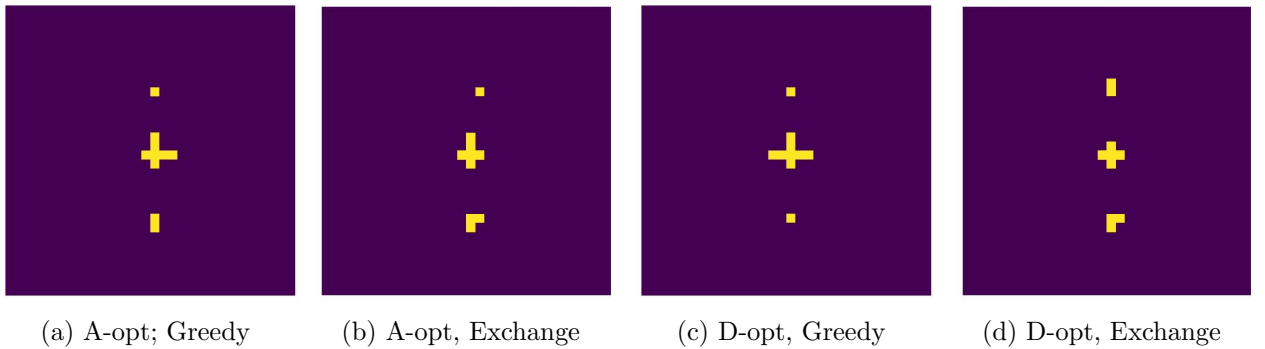


Figure 5: Masks for a budget of $N_S = 10$ frequencies.

3.5 Conventional masks

The OED-based masks are compared here with some of the conventional undersampling masks; see e.g., [9]. Specifically, we show a pseudo-random Gaussian pattern as well as a “circle”

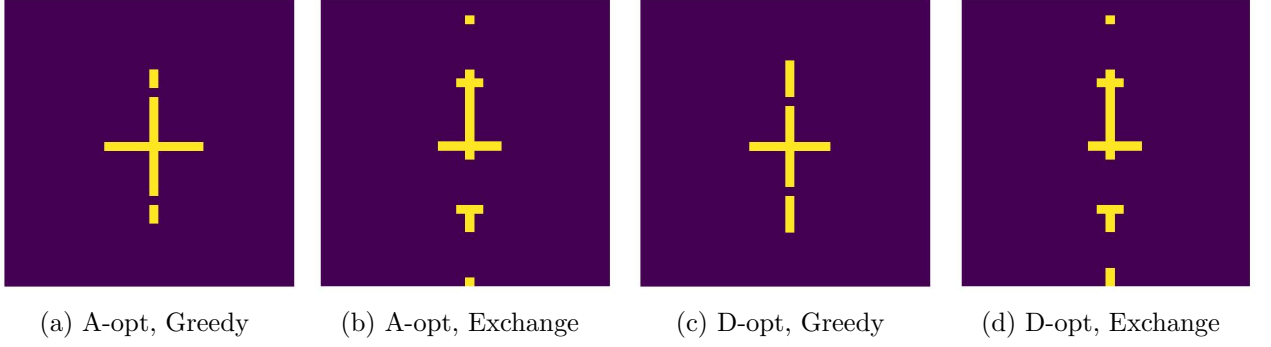


Figure 6: Masks for a budget of $N_S = 25$ frequencies.

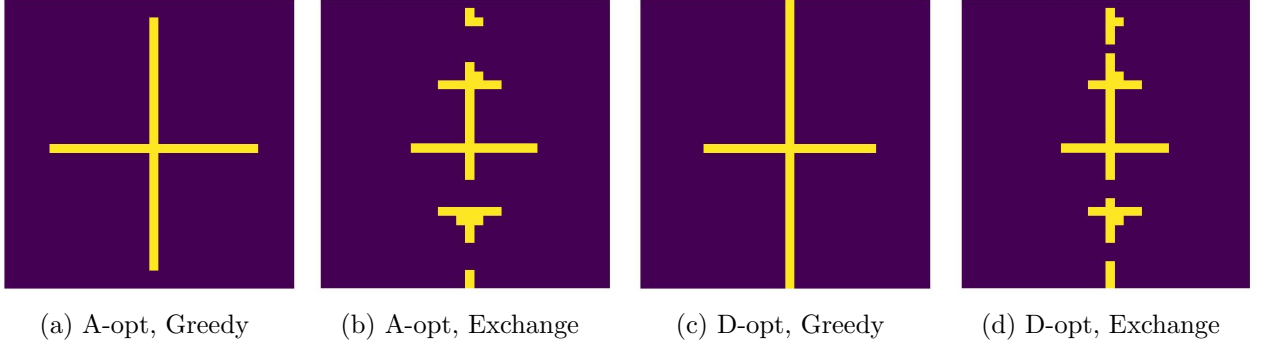


Figure 7: Masks for a budget of $N_S = 50$ frequencies.

pattern that consists of a circle positioned in the middle of the frequency space. Due to the constraints of this design, it was not always possible to match the budgets exactly, but they are off by at most one point. Hence the circular masks also occasionally appear more in the shape of a square. The resulting masks are shown in Figure 8.

3.6 Parameter estimation

We generate thirty realizations of Gaussian noise added to undersampled k-space measurements such that the signal-to-noise ratio (SNR) is 15, amounting to $\sigma_y \approx 5.69$. The parameters are estimated by using ROUKF as discussed in Section 2.2. Because the polynomial is not time-dependent, only a single step is performed; however, we iterate the estimation ten times by providing the result of the previous iteration as the new initial parameter value for the next iteration of the filter. The true solution is provided to the filter as the initial guess. The standard deviation of the noise σ_y is provided to the filter in this case as well, as there is no frame with close-to-zero signal to estimate it from.

Figure 9 shows the quality of the inference results in terms of the relative error of the estimated parameter θ with respect to the true parameter values θ_{true} , that is $e = \frac{\|\theta - \theta_{true}\|}{\|\theta_{true}\|}$. It can be seen that the optimal designs perform considerably better than the conventional designs, even outperforming conventional designs with a higher budget. The variance is also noticeably lower for the optimal masks. There appear to be only minor differences between the two criteria (well within the variance), though the A-optimal masks achieve lower error values than the D-optimal masks in some cases. While the differences between the two algorithms are minor for the higher budgets, for lower budgets it can be seen that the exchange algorithm results in decreased errors and variances for both optimality criteria.

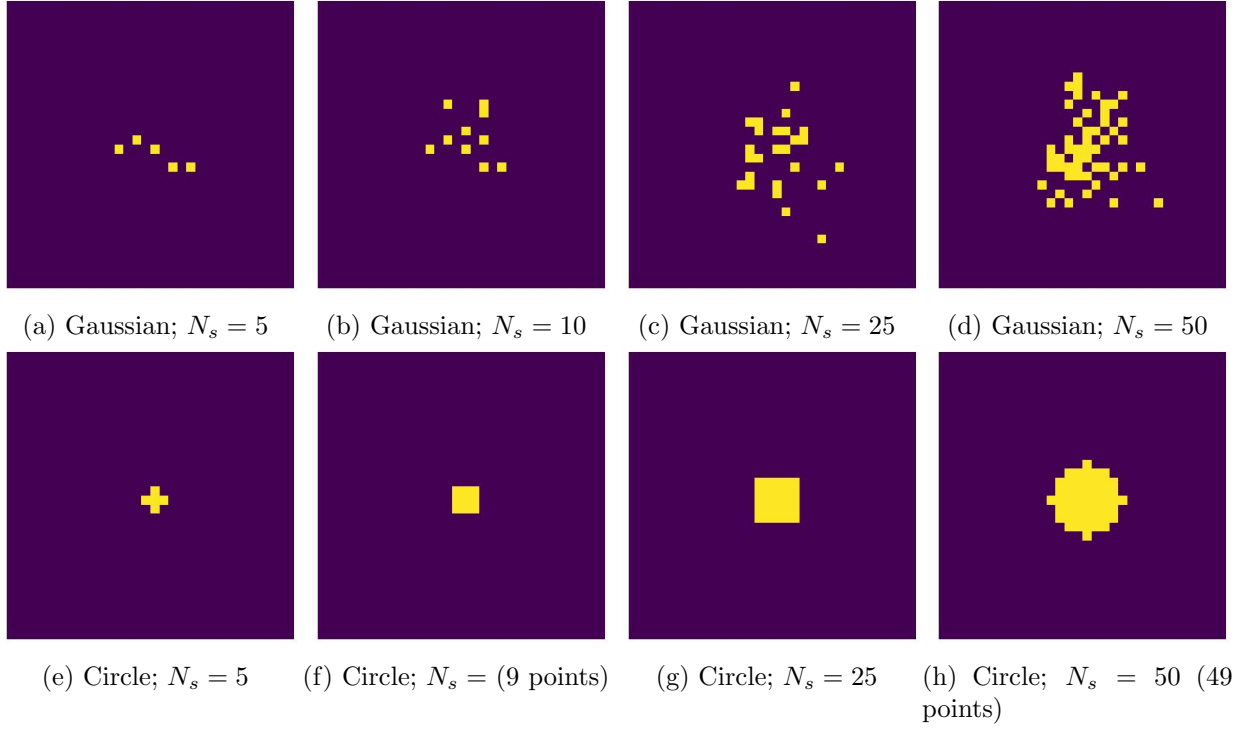


Figure 8: Masks generated using a pseudo-random Gaussian sampling pattern and a circular sampling pattern, for a variety of acceleration factors in the analytical test case (16).

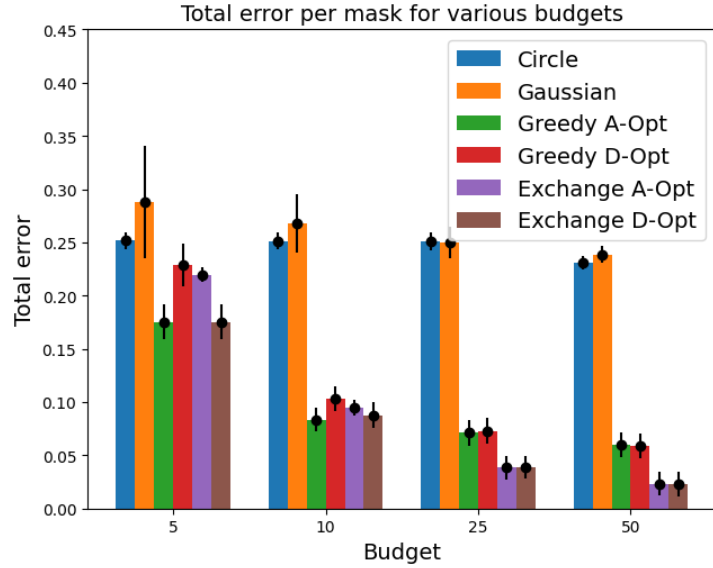


Figure 9: Total error $e = \frac{\|\theta - \theta_{true}\|}{\|\theta_{true}\|}$ of the estimated parameters θ by employing the A- and the D-optimal masks, as well as the circle and the Gaussian masks. Results are shown for various budgets N_s for the analytical test case (16).

In Figure 10, the estimated values of each coefficient of the function are displayed for the different masks and budgets. It can be seen that the variance is noticeably lower for the optimal masks compared to the Gaussian masks, and comparable or slightly lower compared to the circle masks. The largest variances can be observed for parameter 1, and the lowest for parameter 3. This appears to be consistent between the masks.

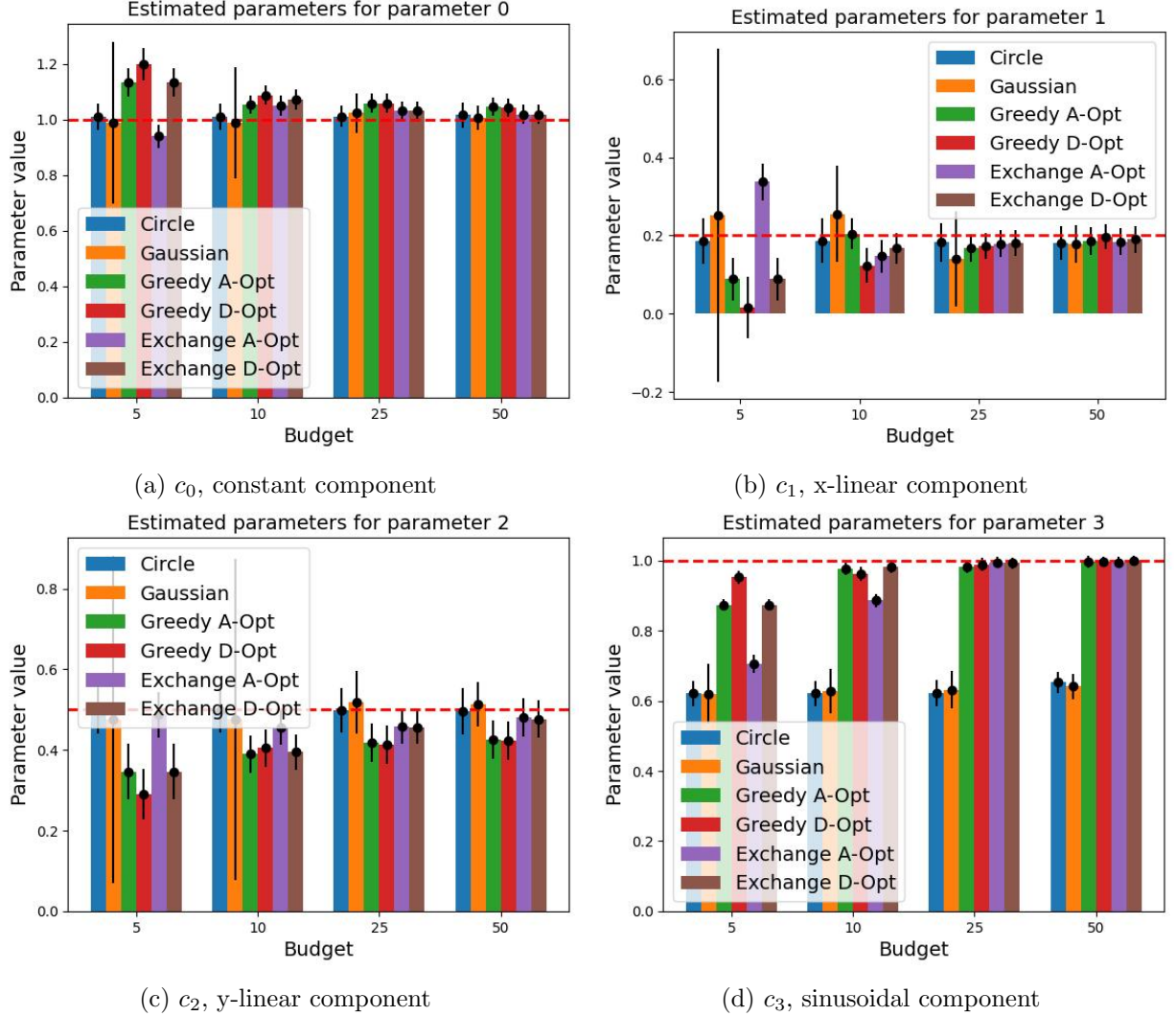


Figure 10: Estimated values of the parameters for different masks averaged over the noise realizations. Red dashed lines indicate true values of the parameters in the analytical test case (16). For visibility, the variance indicated by the black bars has been multiplied by 3.

We plot the sum of the variances of the estimated parameters in Figure 11. As expected, this shows good agreement between a lower criterion value and a lower variance. The differences in the performance of the different masks are noticeable, with the conventional mask performing better for the constant and linear components for lower budgets, but highly underestimating the coefficient of the sine function even for the highest budget. This is likely because neither the circle nor the Gaussian includes the $k = (0, \pm 7)$ frequency, which has the highest sensitivity for that parameter. Conversely, the optimal masks estimate this parameter well even for lower budgets. Therefore there are less points included in these masks that are relevant for the constant and linear components, thus there is a higher error for these parameters for the low

budgets.

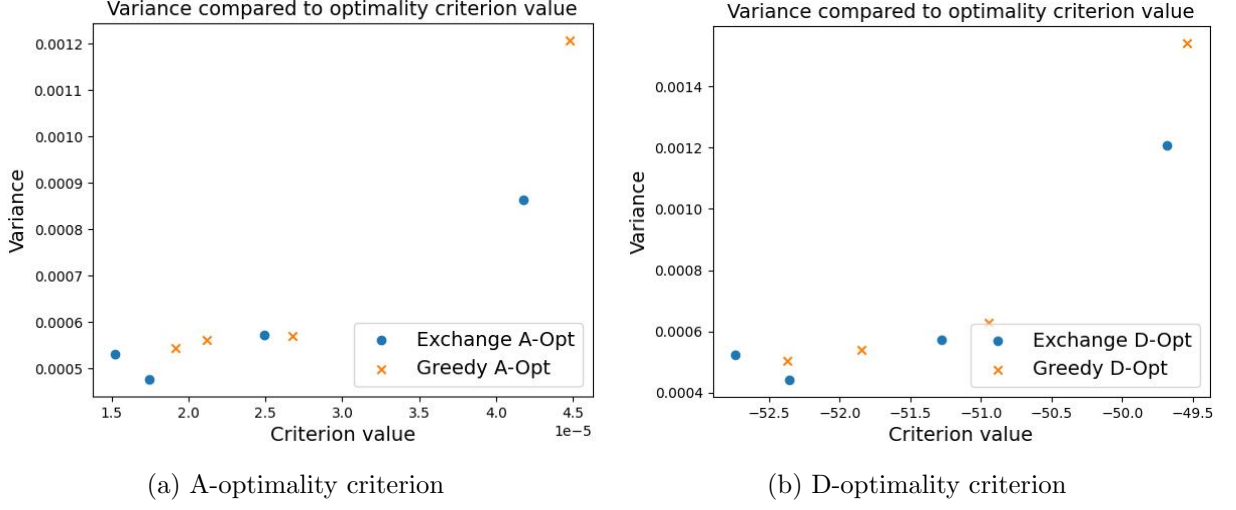


Figure 11: Optimality criterion values compared to the sum of the variances of the estimated parameters in the analytical test case (16). A lower optimality criterion value is better.

It is worth noting that none of the optimality criteria optimize directly for the accuracy of the estimated parameters. In Figure 12, we therefore plot the optimality criterion values against the error for each set of optimal masks and the conventional masks. It can be seen that there is a strong trend: a better criterion value (lower for both the A- and D-criteria) generally leads to a lower error, especially for the lower budgets. For higher budgets, there are occasional outliers where a higher criterion value nonetheless corresponds to a lower error. It can also be seen that the exchange algorithm achieves better criterion values than the greedy algorithm.

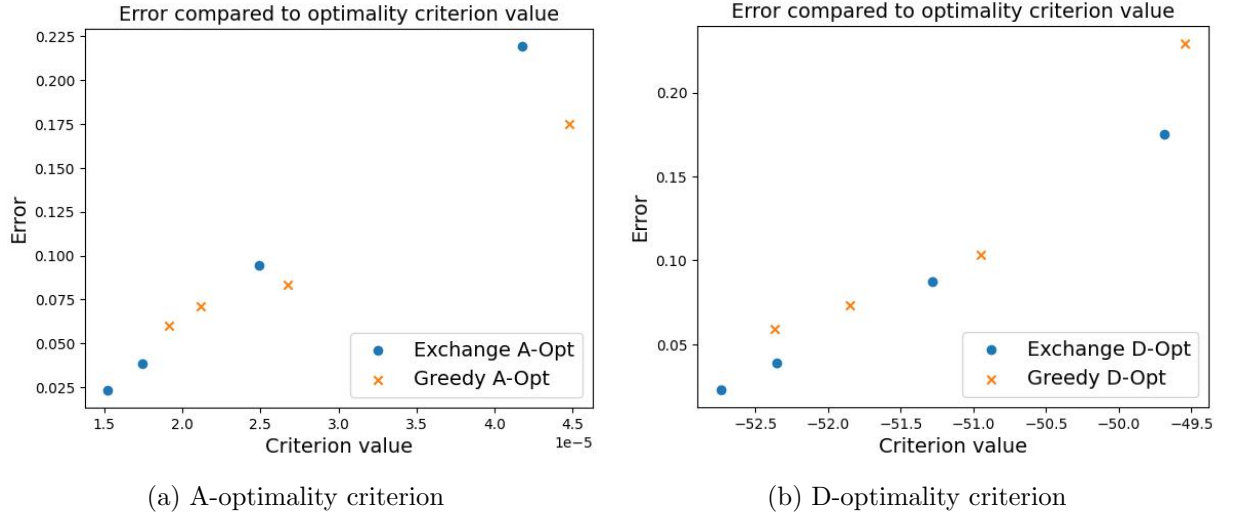


Figure 12: Optimality criterion values compared to the errors in the analytical test case (16). A lower optimality criterion value is better.

3.7 Using sensitivities for estimated parameter values

So far, we have calculated the sensitivities using the true parameters. However, generally these values will not be available. Therefore we now consider sensitivities computed with incorrect parameter values, those being $c_0 = c_1 = c_2 = c_3 = 0.1$.

The optimal masks computed with these sensitivities generally often coincide with at least one mask computed with the true sensitivities, and differ only slightly otherwise. The results of the inverse problem, for the true and approximated sensitivities, are shown in Figure 13. It can be seen that there are rarely significant differences due to the sensitivities.

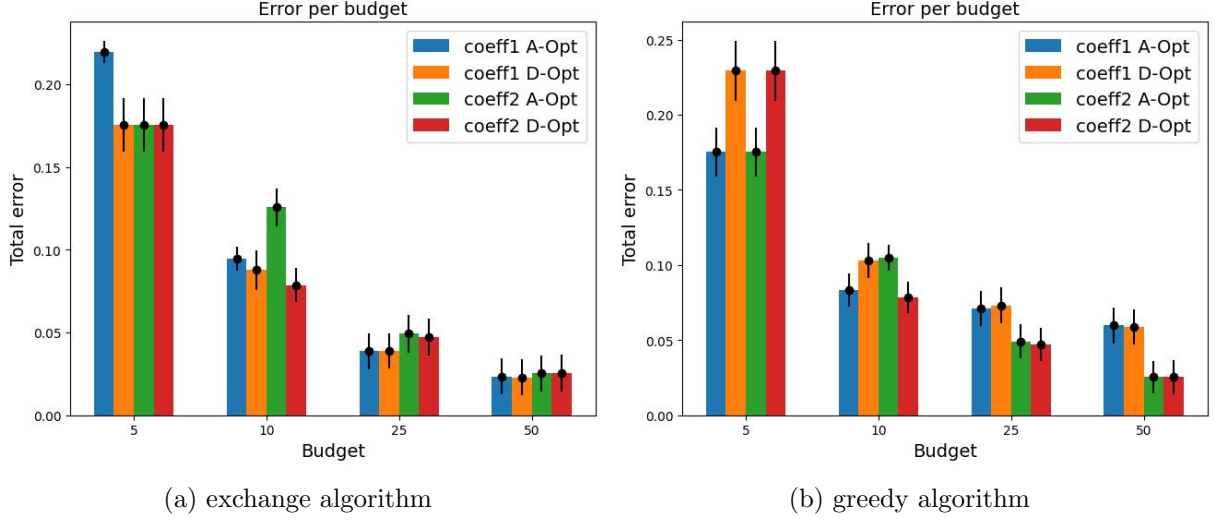


Figure 13: Comparison of the error of the inverse problem between the sensitivities computed with two different sets of coefficients, $\text{coeff1} = [1.0, 0.2, 0.5, 1.0]$, which are the true values, and $\text{coeff2} = [0.1, 0.1, 0.1, 0.1]$.

As can be seen from these results, using masks computed by OED algorithms, regardless of criterion, identify the significant frequencies and provide large improvements in terms of error and variance in the parameters estimated by the inverse problem. We will therefore now test our approach in a more realistic application.

4 Aortic Hemodynamics Test Case

4.1 Forward model

We use the same model and process as is used in [9]. We consider a geometry of the lumen of the ascending and descending aorta including the outlets of the brachycephalic artery, left common carotid artery, and left subclavian artery, as depicted in Figure 14. This geometry serves as the domain for the forward model. The geometry was discretized with unstructured trapezoidal elements with a total of 20,916 points. The boundary of the geometry consists of six different boundaries: Γ_{in} being the inlet boundary in the ascending aorta, Γ_w the arterial wall, and the remaining boundaries Γ_l for $l = 1, \dots, 4$ representing the outlets.

We model the blood flow in this domain with the incompressible Navier-Stokes equations for the velocity $\mathbf{u}(\mathbf{x}, t) \in \mathbb{R}^3$ and the pressure $p(\mathbf{x}, t) \in \mathbb{R}$:

$$\rho \frac{\partial \mathbf{u}}{\partial t} + \rho(\mathbf{u} \cdot \nabla) \mathbf{u} - \mu \Delta \mathbf{u} + \nabla p = 0 \text{ in } \Omega \quad (17a)$$

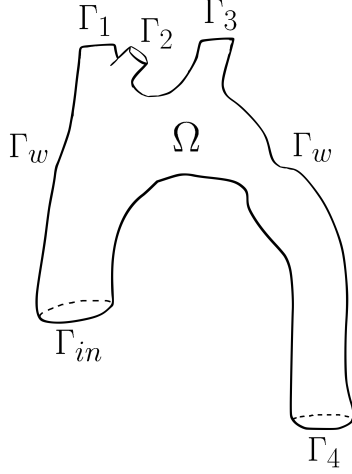


Figure 14: 3D aortic model geometry

$$\nabla \cdot \mathbf{u} = 0 \text{ in } \Omega \quad (17b)$$

$$\mathbf{u} = \mathbf{u}_{in} \text{ on } \Gamma_{in} \quad (17c)$$

$$\mathbf{u} = \mathbf{0} \text{ on } \Gamma_w \quad (17d)$$

$$\mu \frac{\partial \mathbf{u}}{\partial \mathbf{n}} - p \mathbf{n} = -P_l(t) \mathbf{n} \text{ on } \Gamma_l \quad (17e)$$

with ρ, μ the density and dynamic viscosity of the fluid and $P_l(t)$ being given by a Windkessel boundary condition defined by:

$$P_l = R_{p,l} Q_l + \pi_l \quad (18a)$$

$$Q_l = \int_{\Gamma_l} \mathbf{u} \cdot \mathbf{n} \quad (18b)$$

$$C_{d,l} \frac{d\pi_l}{dt} + \frac{\pi_l}{R_{d,l}} = Q_l \quad (18c)$$

This boundary condition models the effects of the remaining vascular system on the outlet via the proximal and distal resistances R_p, R_d of the vasculature and the distal compliance C_d of the vessels. Lastly, the inflow \mathbf{u}_{in} is defined as

$$\mathbf{u}_{in} = -U f(t) \mathbf{n},$$

where U is a constant amplitude and

$$f(t) = \begin{cases} \sin(\frac{\pi t}{T}) & \text{if } t \leq T, \\ \frac{\pi}{T}(t - T) \exp^{-k(t-T)} & \text{if } T_c > t > T, \end{cases}$$

with $T_c = 0.8$ and $T = 0.36$. The physical parameters are set as seen in Table 2. The forward problem is solved using an in-house finite elements solver, with a semi-implicit 3D-0D coupling scheme as in [17], using $P1$ elements for both the velocity and the pressure and a time step of $dt = 1 \text{ ms}$. The full algorithm is detailed in the appendix Appendix A.

Parameter	Value
ρ ($gr \cdot cm^3$)	1.2
μ (P)	0.035
U ($cm \cdot s^{-1}$)	75
T_c (s)	0.80
T (s)	0.36
κ (s^{-1})	70

	Γ_1	Γ_2	Γ_3	Γ_4
R_p ($dyn \cdot s \cdot cm^{-5}$)	480	520	520	200
R_d ($dyn \cdot s \cdot cm^{-5}$)	7200	11520	11520	4800
C ($dyn^{-1} \cdot cm^5$)	$4 \cdot 10^{-4}$	$3 \cdot 10^{-4}$	$3 \cdot 10^{-4}$	$4 \cdot 10^{-4}$

Table 2: Physical parameters and numerical values of the three-element Windkessel parameters for every outlet.

4.2 Measurement problem

The forward solution is undersampled in time to $dt_{meas} = 15 ms$, resulting in a total of 56 measurements of the velocity. From the solution of the forward problem, we simulate a PC-MRI acquisition by sub-sampling onto a rectangular domain meshed in a structured fashion with a resolution of $2 mm$ in all three spatial directions, and then applying the process described in Equation (5) with a $venc$ of twice the maximal velocity. The magnitude is modeled as

$$M(\mathbf{x}) = \begin{cases} 1.0 & \text{if } \mathbf{x} \text{ is in the lumen of the vessel,} \\ 0.5 & \text{otherwise.} \end{cases} \quad (19)$$

and the background phase was set to an arbitrary constant value of $\phi_{back} = 7.5 \cdot 10^{-2} rad$.

The unknown parameters are taken to be the inflow U and the distal resistances $R_{d,i}$ of the Windkessel outlets $\Gamma_1, \Gamma_2, \Gamma, 3$. We have decided to optimize only a two-dimensional mask in the $x - y$ -plane and “stack” these masks for the z -dimension, which is a common approach for 3D MRI acquisitions. We are also using the same masks for all velocity directions. Finally a complex Gaussian noise $\epsilon \in \mathbb{C}^N$ is added with a signal-to-noise ratio (SNR) of 15. Fifty independent realizations of the noise were generated.

4.3 Sensitivities

The sensitivities for each parameter are computed numerically using a first-order difference scheme with a relative difference of $h = 10^{-6}$. The magnitude of the sensitivities for each parameter for a slice at $z = 0$ is shown in Figure 15. It is already evident that the sensitivities of the parameters follow different patterns, with those of the inflow U especially focused on the center while those of the Windkessel resistances spread out more. Note also that the sensitivity of U is several orders of magnitude larger than the other sensitivities. Due to this, as well as the inflow usually being much more robust in estimation than the Windkessel parameters, we have chosen to use only the sensitivities of the three Windkessel resistances for the construction of the optimal masks.

4.4 Implementation of the optimization algorithm

We create masks for the same four budgets of points $N_s = 5, 10, 25 \text{ and } 50$ (in the 2D mask, hence more points in the complete 3D mask) which now corresponds to acceleration factors $R \sim 211, 106, 42, 21$, respectively.

We are using the same implementation as for the analytic test case. The compute times are listed in Table 3. With the higher computational cost per computation of the FIM, the advantage of the greedy algorithm is now evident for all budgets except the lowest one. Especially for

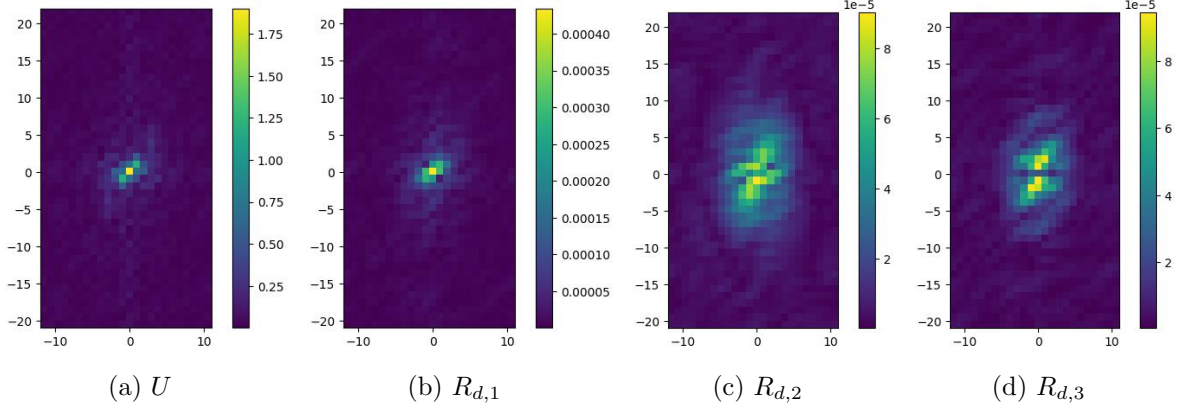


Figure 15: Magnitudes of the sensitivities of the measurement to each of the parameters in the aorta test case. Note the different scales shown in the color bars.

the highest budget, the exchange algorithm requires several hours to complete for all three parameters, whereas the greedy algorithm finishes after a few minutes.

Algorithm	1 parameter				3 parameters			
	5	10	25	50	5	10	25	50
Greedy	8.92s	28.93s	1min53s	3min56s	9.32s	19.78s	1min07s	4min 34s
Exchange	1.1s	27.38s	1min28s	1h07min	10s	1min 38s	27min27s	2h18min

Table 3: Computing times for the two algorithms for different budgets on the aorta testcase

4.5 Optimal masks

The optimal masks corresponding to the selected budgets are shown in Figures 16—19. Overall, the optimal masks have an tilted, elliptic shape, populating the center of the k-space. For the budgets of 5 and 10 points, considerable differences between the results of the different algorithms can be seen. For the higher budgets, all generated masks are near-identical, and even for the lower budgets, the A- and D-optimal masks are often identical.

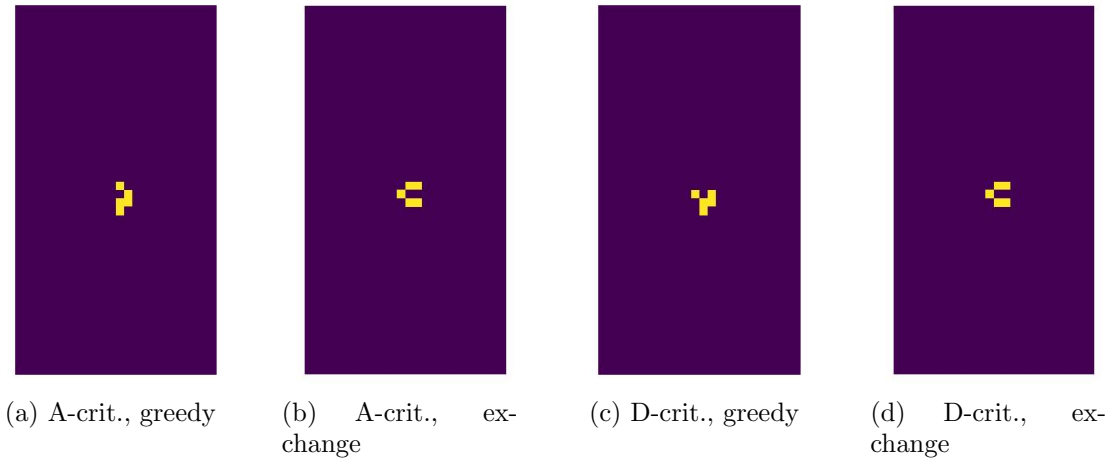


Figure 16: Masks for a budget of $N_S = 5$ frequencies.

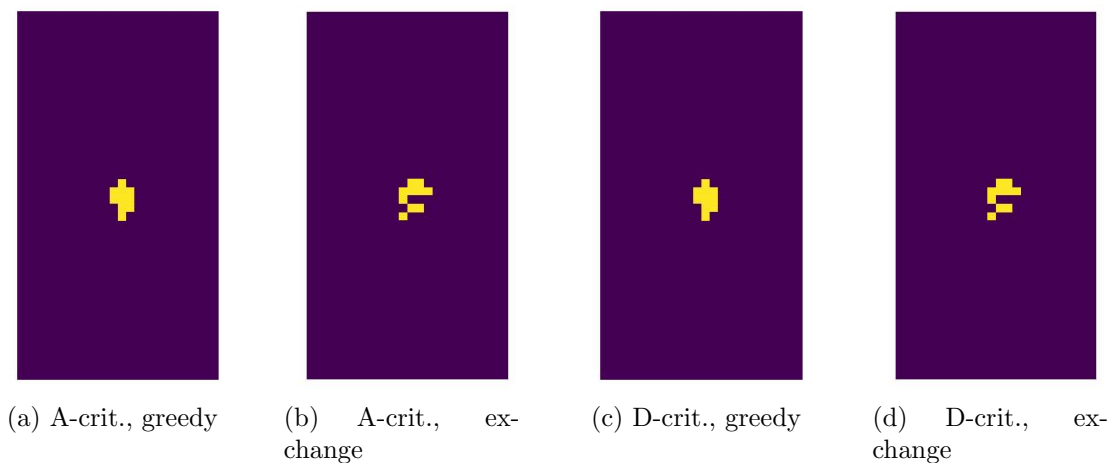


Figure 17: Masks for a budget of $N_S = 10$ frequencies.

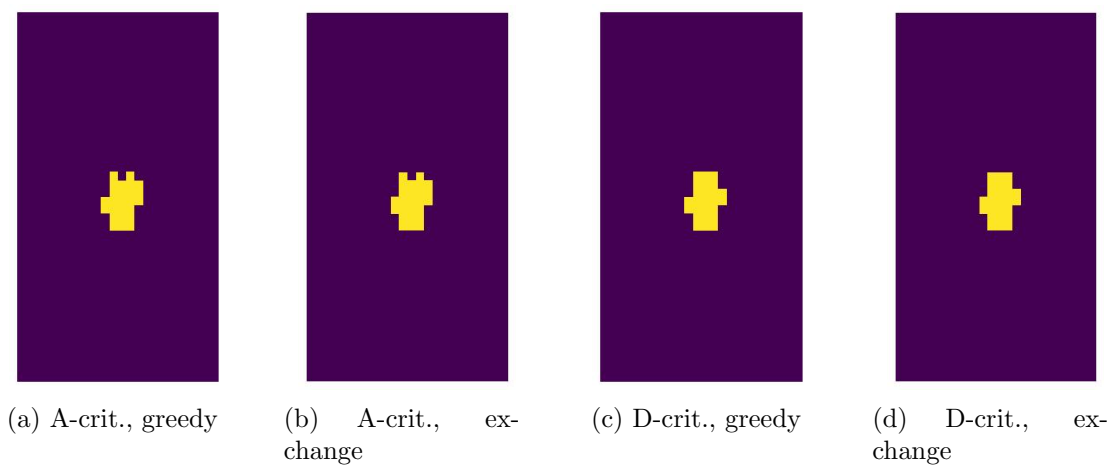


Figure 18: Masks for a budget of $N_S = 25$ frequencies.

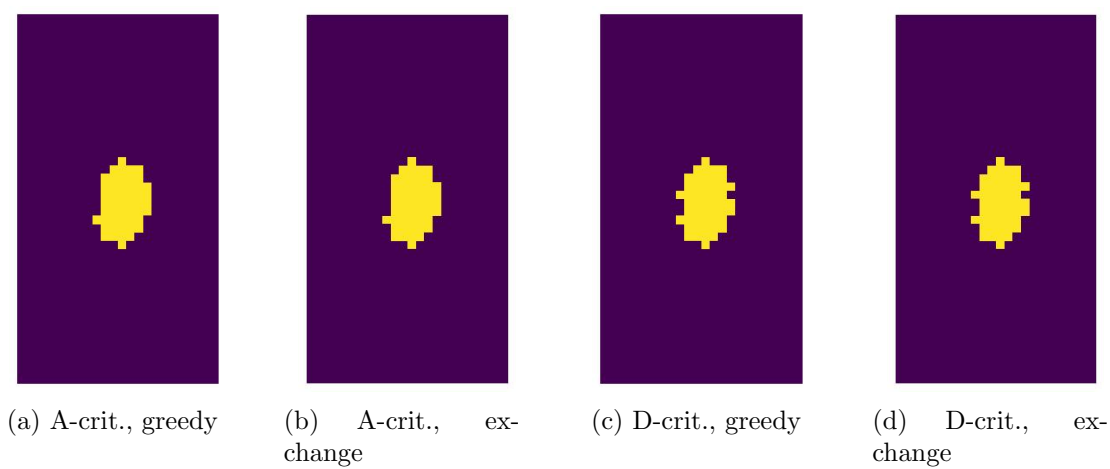


Figure 19: Masks for a budget of $N_S = 50$ frequencies.

4.6 Conventional masks

We are again using the “circle” and the pseudo-random Gaussian pattern for comparison, which are shown in Figure 20.

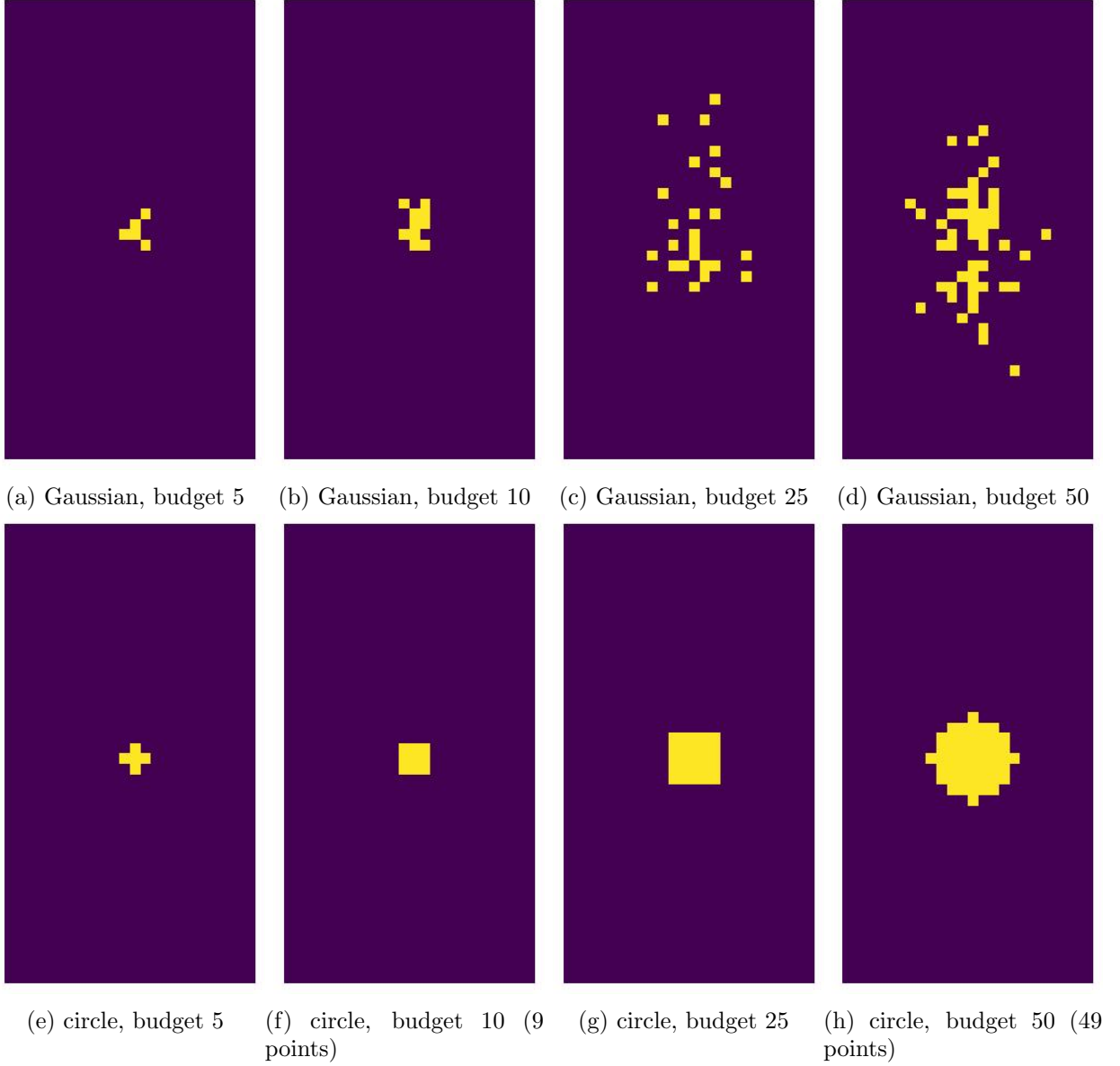


Figure 20: Masks generated using a pseudo-random Gaussian sampling pattern and a circular sampling pattern, for a variety of acceleration factors, for the aorta test case.

4.7 Parameter estimation

In this case we generate fifty independent noise realizations with an SNR of 15 and use ten iterations of the ROUKF, each time using the result of the last iteration as the new initial guess of the next, but resetting the standard deviation of the parameters. The true values are $R_{d,1} = 7200$, $R_{d,2} = 11520$, $R_{d,3} = 11520$, while the initial values provided to ROUKF were $R_{d,1} = 4000$, $R_{d,2} = 4000$, $R_{d,3} = 4000$.

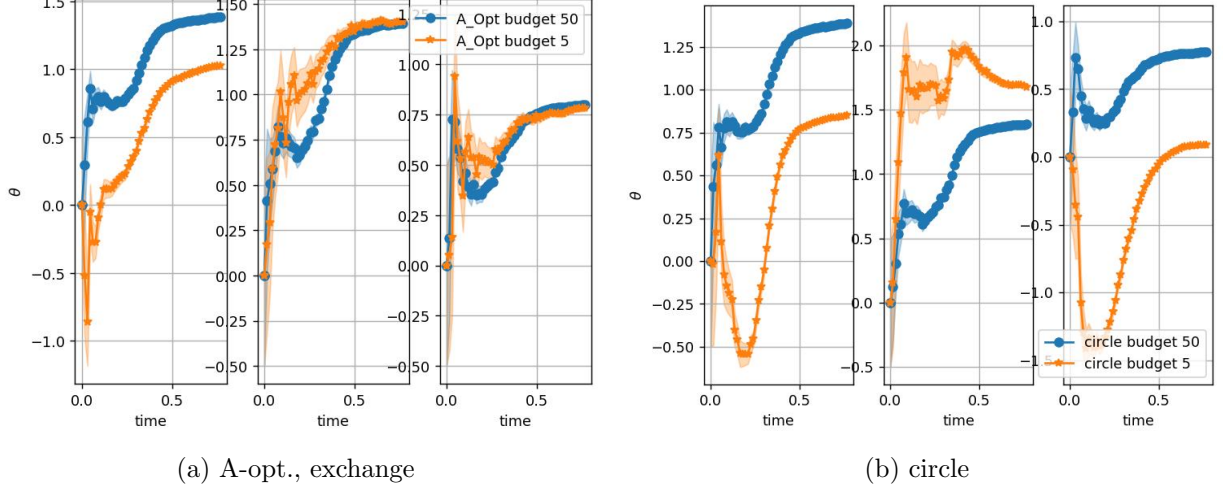


Figure 21: Evolution of the parameters over time during the first iteration of the ROUKF, for two different budgets.

We show the parameter evolution curves of the ROUKF algorithm for the circle mask and the A-optimal mask with the exchange algorithm in Figure 21 for the first ROUKF iteration. It can be seen that the curves for a lower budget contain more and higher spikes in either direction before converging, for either mask. While both curves qualitatively follow the same shape, it can be seen that the curves for the circle mask do not reach the same values, indicating a difference in assimilated information. Meanwhile, the curves for the optimal masks remain much closer throughout the entire time. This seems to indicate a smaller loss of information due to still selecting the most information-dense points.

The total error $e = \frac{\|\theta - \theta_{true}\|}{\|\theta_{true}\|}$ of the three estimated parameters, for all four budgets and the circle, Gaussian, and all different optimal masks, are shown in Figure 22. For all budgets, but especially for the lower budgets, the optimal masks considerably outperforms the conventional masks in terms of error. The variance of the error of the parameter estimates remains similar between the different masks.

Comparing the different algorithms, there is no difference for the higher budgets (25 and 50) as here both algorithms led to the same mask. For the lower budgets, however, there is a notable advantage in using the exchange algorithm over the greedy algorithm. There are only minimal differences in the results between the A- and D- optimal masks. The exception is for a budget of 5 points, where a single point being in a different position in the masks identified by the greedy algorithm does lead to a higher error for the A-optimal mask.

We can observe the error standard deviation consistently decreases when increasing the budget, as expected. The error mean also decreases, with a single exception of the exchange algorithm when increasing the budget from 10 to 25. Though we have no clear explanation about this result, a possible explanation could be that the additional selected frequencies lead to a cost function with a local minimum that is closer to the initial guess, hence making the ROUKF algorithm converge to such result.

We display the estimated values of each parameter for the different masks and budgets in Figure 23. Both qualitatively and quantitatively, these results conform with the observations above. The difference in performance between the optimal masks and the conventional masks is more pronounced for $R_{d,1}$ and $R_{d,3}$ than $R_{d,2}$, though, which could indicate an advantage of the optimal masks especially in estimating difficult parameters (as those parameters correspond to smaller outlets compared to $R_{d,2}$, and are therefore in our experience harder to estimate

accurately).

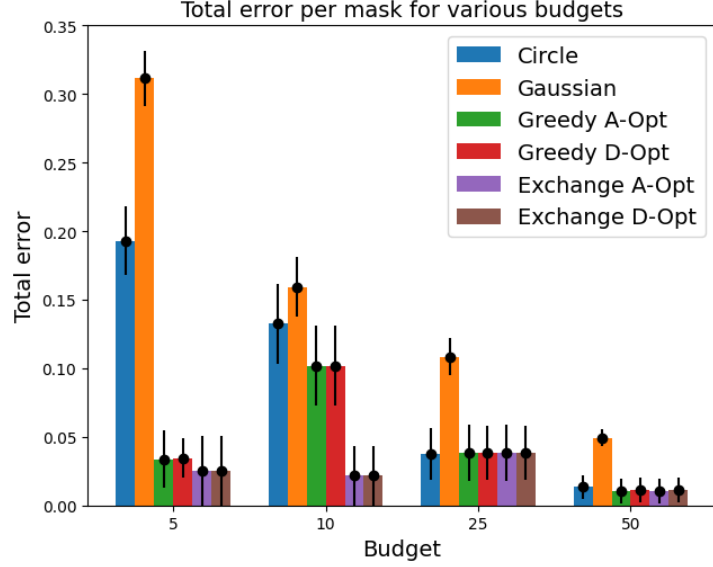


Figure 22: Total error of the Windkessel parameters estimated in the inverse problem for the A-optimal and D-optimal masks, as well as the circle and Gaussian masks, for various budgets.

We also plot the error and the sum of the variances against the criterion value in Figures 24, and 25, respectively. The visible trend confirms the relation between the criteria value and the outcome of the inverse problem also in this more complex test case.

4.8 Using sensitivities for estimated parameter values

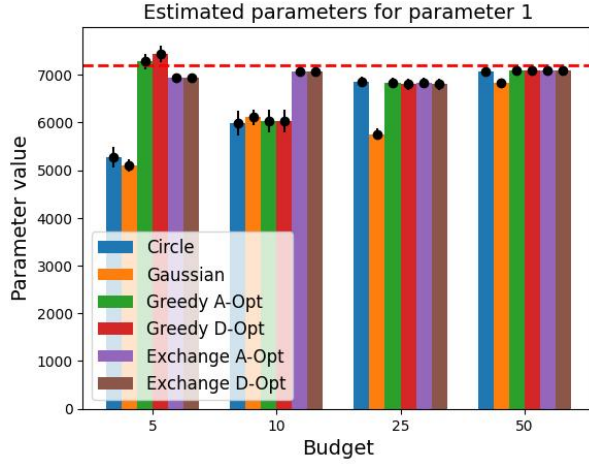
Here as well we consider sensitivities computed with incorrect parameter values, in this case, the same ones as the ones used as the initial guess for the inverse problem.

The optimal masks computed with these sensitivities, like for the analytical test case (16), often agree with those computed with the true sensitivities. The results of the inverse problem using the masks, for the true and approximated sensitivities, are shown in Figure 26. It can be seen that using the approximated sensitivities does not lead to significantly different results. The process therefore seems robust to the exact parameter values used for the computation of the sensitivities, at least within a realistic range.

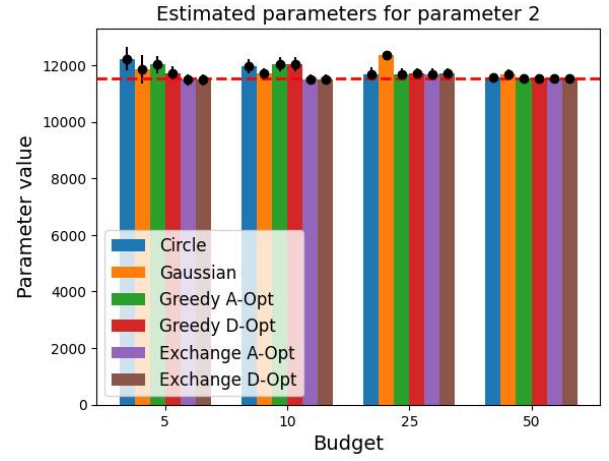
The exception is the A-optimal greedy mask for the lowest budget, which shows a considerably higher error when using sensitivities generated with approximated values. The masks for this case, as well as the corresponding masks with the accurate sensitivities, are shown in Figure 27, and are one of the few sets of masks that differ notably based on the change in the sensitivities. Therefore for very low budgets, with approximated sensitivities, the exchange algorithm may be a more reliable choice. Nevertheless, even in this case the error for the greedy mask is less than for a conventional mask.

5 Discussion

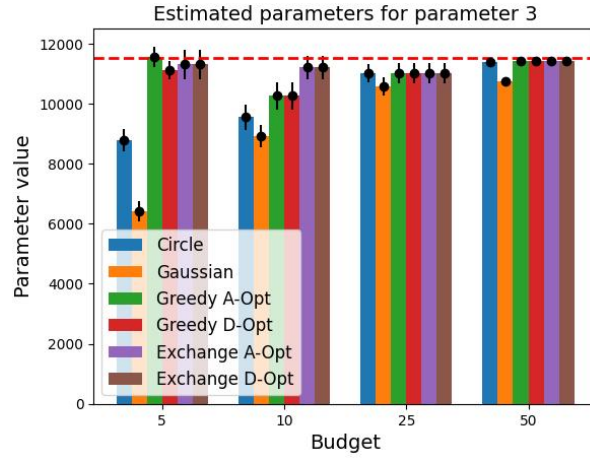
The numerical results are generally consistent between the analytical test case and the aorta test case. The optimal masks outperform the conventional masks in terms of both error and variance in nearly every case, for both optimality criteria and for either optimization algorithm.



(a) Parameter 1

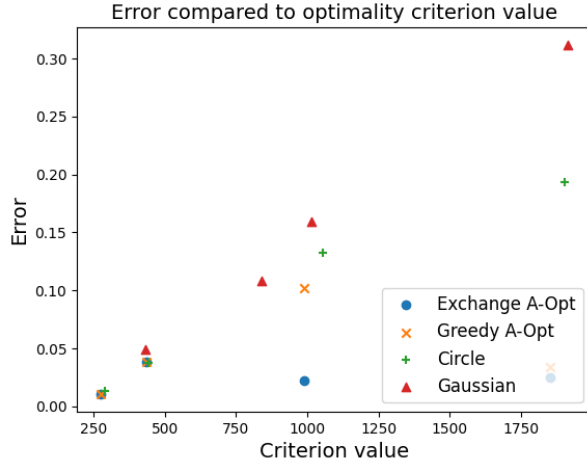


(b) Parameter 2

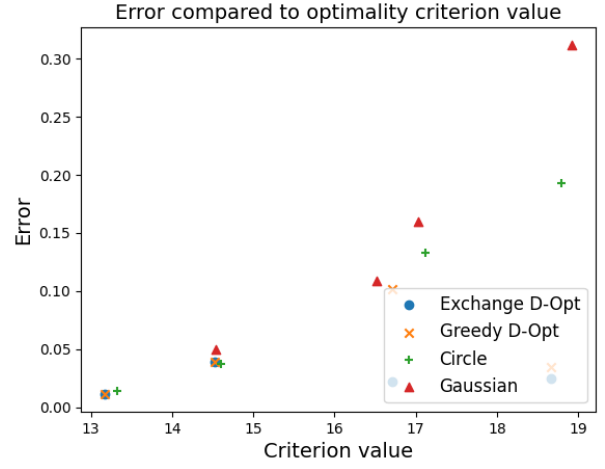


(c) Parameter 3

Figure 23: Estimated values of the Windkessel parameters for different masks. Red dashed lines indicate true values of the parameters.

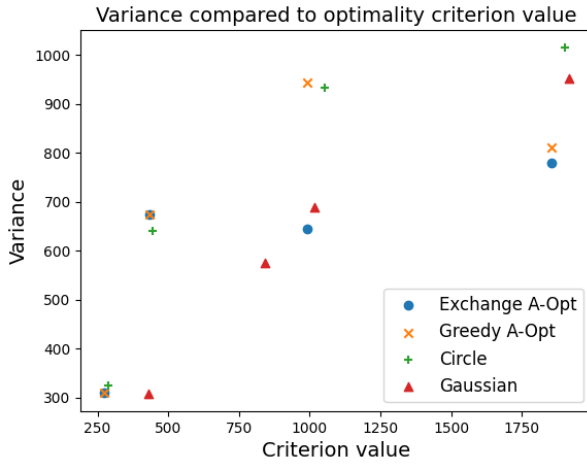


(a) A-optimality criterion

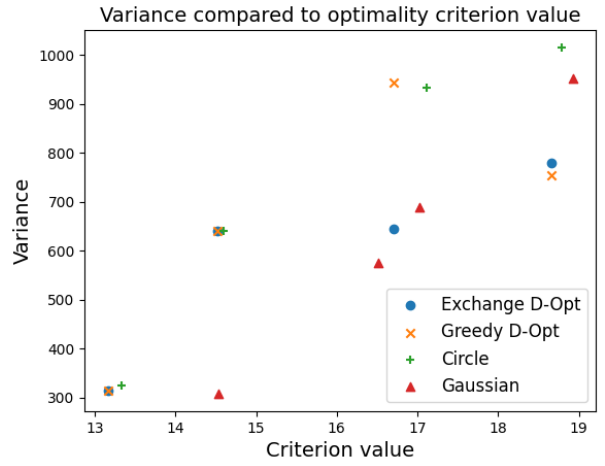


(b) D-optimality criterion

Figure 24: Optimality criterion values compared to the errors of the estimated parameters in the aorta test case. A lower optimality criterion value is better. Due to overlaps, not all points may be clearly visible.



(a) A-optimality criterion



(b) D-optimality criterion

Figure 25: Optimality criterion values compared to the sum of the variances of the estimated parameters of the aorta test case. A lower optimality criterion value is better. Due to overlaps, not all points may be clearly visible.

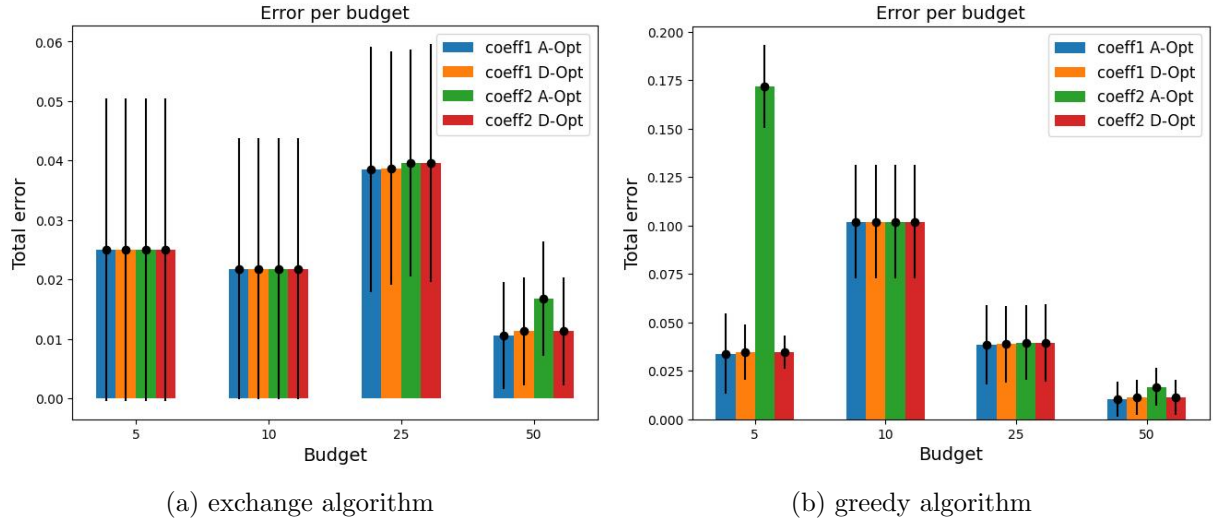


Figure 26: Comparison of the error of the inverse problem between the sensitivities computed with the true parameter values and the incorrect parameter values.

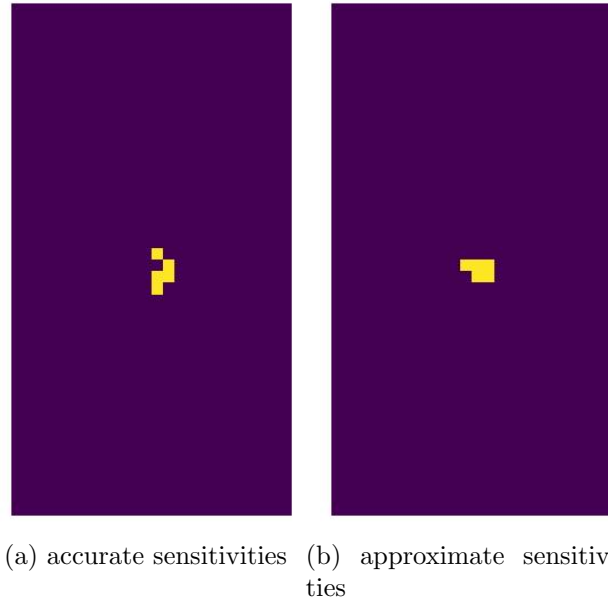


Figure 27: A-optimal masks optimized with the greedy algorithm, for sensitivities computed with the true parameter values and with incorrect parameter values.

The results for the aorta test case are more similar between criteria and algorithms, which may be due to the different nature of the underlying signal. As a result, no clear preference between the optimality criteria is apparent. Other optimality criteria could be explored, which may have a better relation to the error of the estimated parameters. A criterion such as the c-criterion, which optimizes based on a predetermined linear combination of the parameters, could also be used to account for differences in the scale of the sensitivities for different parameters [15].

Other optimization methods should be explored as well, since the exchange algorithm may be unfeasible for an increased number of parameters or higher data resolution, and the greedy algorithm may not lead to an optimal solution, especially for more complex problems. A potential solution could be to initialize the exchange algorithm with the results of the greedy algorithm, and therefore potentially cut down on the number of exchanges required compared to a randomly initialized mask, or to use a more optimized version of the algorithm. Another option may be to use probabilistic/stochastic algorithms [18, 19] to find the optimal design by iteratively sampling from the distribution. Alternatively, if this is computationally unfeasible, we could relax the constraint of having a discrete design and instead consider a function of weights in $[0, 1]^N$ such that they sum up to 1, leading to a continuous optimization problem. This raises additional questions about how to round the resulting continuous design to obtain a discrete design, and may also not result in the optimal discrete design; see e.g., [20].

An alternative approach would be to work with a parametrizable family of masks, with additional constraints to ensure they result in a valid sampling pattern [21]. However, this would only provide an optimal design within this family of masks.

Additionally, a further exploration of the effects of the assumed parameters for the computation of the sensitivities is needed, as it is likely that the computed design holds only within a range of coefficients which are close enough. This uncertainty in the coefficients and therefore in the sensitivities can also be included in the optimal design process, using techniques such as in [12, 22].

One limitation of the numerical analysis carried out in this paper is the lack of real data. Real MRI data generally includes measurements taken by different magnet coils. Due to their different positioning, these coils generally have a different ability to detect the signal in the field-of-view, which is often non-uniform in space as well. This is often shown in the form of a "coil sensitivity map", which describes how well a particular coil captures the signal in a specific voxel. The effect of taking measurements with these differing coil sensitivities will likely have to be accounted for. Additionally, the magnitudes and background phases can vary in time and space as well, which may need to be considered in the computation of the measurement sensitivities for the optimal design process. As our method requires the magnitude and the background phase, it will have to be explored whether the measurement sensitivities computed with estimations or modelled versions result in sufficiently good optimal designs. We plan to address this in future research.

6 Conclusion

In this work, we have introduced an Optimal Experimental Design (OED) framework for the selection of k-space sampling patterns tailored to parameter estimation in inverse hemodynamics problems. Through both analytical and aortic hemodynamics test cases, we demonstrated that masks optimized using OED criteria (A- and D-optimality) consistently outperform conventional sampling patterns in terms of parameter estimation accuracy and variance, especially for high undersampling (acceleration factor $R \approx 200$). The optimal masks achieve lower errors with a budget of 5 points per slice than the conventional masks with a budget of 50, thus providing a speed-up of over $10\times$ in terms of the acquisition time in the flow encoding directions. The results

also show that the choice of optimization algorithm can impact performance for low sampling budgets, with the exchange algorithm providing some advantage over the greedy approach in these cases, but at a higher computational cost.

Our findings indicate that OED-based mask design is a promising strategy for accelerating MRI acquisitions while maintaining or improving the quality of parameter estimates in cardiovascular modeling. Though further research is needed, the approach is robust to moderate inaccuracies in the assumed parameter values used for sensitivity calculations, and the optimality criteria correlate well with actual estimation errors. Future work should address the integration of more advanced optimization algorithms, the extension to real MRI data with coil sensitivities, and the incorporation of parameter uncertainty into the design process to further enhance the practical applicability of this framework.

Acknowledgments

C.B. and M.L. acknowledge the funding from the European Research Council (ERC) under the European Union’s Horizon 2020 research and innovation program (grant agreement No 852544 - CardioZoom). A. A. was supported by the Applied Mathematics activity within the U.S. Department of Energy, Office of Science, Advanced Scientific Computing Research, under Contract DEAC02-06CH11357.

References

- [1] Michael Markl, Alex Frydrychowicz, Sebastian Kozerke, Mike Hope, and Oliver Wieben. 4D flow MRI. *Journal of Magnetic Resonance Imaging*, 36(5):1015–1036, 2012. tex.publisher: Wiley Online Library.
- [2] Joost van Schuppen, Annelies E. van der Hulst, J. Michiel den Harder, Lukas M Gottwald, Raschel D. van Luijk, Josien C. van den Noort, Jules L. Nelissen, Casper F. Coerkamp, S. Matthijs Boekholdt, Paul F.C. Groot, Aart Nederveen, Pim van Ooij, R. Nils Planken, and Delphi Panel Members. Prerequisites for Clinical Implementation of Whole-Heart 4D-Flow MRI: A Delphi Analysis. *Journal of Magnetic Resonance Imaging*, 61(4):1618–1628, 2025.
- [3] Aparna Sodhi, Michael Markl, Andrada R. Popescu, Lindsay M. Griffin, Joshua D. Robinson, and Cynthia K. Rigsby. Highly accelerated compressed sensing 4D flow MRI in congenital and acquired heart disease: comparison of aorta and main pulmonary artery flow parameters with conventional 4D flow MRI in children and young adults. *Pediatric Radiology*, 53(13):2597–2607, October 2023.
- [4] Akos Varga-Szemes, Moritz Halfmann, U. Joseph Schoepf, Ning Jin, Anton Kilburg, Danielle M. Dargis, Christoph Düber, Amir Ese, Gilberto Aquino, Fei Xiong, Karl-Friedrich Kreitner, Michael Markl, and Tilman Emrich. Highly Accelerated Compressed-Sensing 4D Flow for Intracardiac Flow Assessment. *Journal of Magnetic Resonance Imaging*, 58(2):496–507, August 2023.
- [5] Elisabeth Neuhaus, Kilian Weiss, Rene Bastkowski, Jonas Koopmann, David Maintz, and Daniel Giese. Accelerated aortic 4D flow cardiovascular magnetic resonance using compressed sensing: applicability, validation and clinical integration. *Journal of Cardiovascular Magnetic Resonance*, 21(1):65, 2019.

- [6] Mj Negahdar, Mo Kadbi, Michael Kendrick, Marcus F. Stoddard, and Amir A. Amini. spiral imaging of flows in stenotic phantoms and subjects with aortic stenosis. *Magnetic Resonance in Medicine*, 75(3):1018–1029, March 2016.
- [7] Steven Keckskemeti, Kevin Johnson, Yijing Wu, Charles Mistretta, Patrick Turski, and Oliver Wieben. High resolution three-dimensional cine phase contrast MRI of small intracranial aneurysms using a stack of stars k -space trajectory. *Journal of Magnetic Resonance Imaging*, 35(3):518–527, March 2012.
- [8] Daniel Giese, Tobias Schaeffter, and Sebastian Kozerke. Highly undersampled phase-contrast flow measurements using compartment-based $k - t$ principal component analysis. *Magnetic Resonance in Medicine*, 69(2):434–443, February 2013.
- [9] Miriam Löcke, Pim van Ooij, and Cristóbal Bertoglio. Parameter estimation in fluid flow models from undersampled frequency space data, March 2025. arXiv:2503.04092 [math].
- [10] A C Atkinson, A N Donev, and R D Tobias. *Optimum Experimental Designs, with SAS*. Oxford University PressOxford, 2007.
- [11] Dariusz Ucinski. *Optimal measurement methods for distributed parameter system identification*. CRC press, 2004.
- [12] Valerij V. Fedorov and Peter Hackl. *Model-oriented design of experiments*. Number volume 196 in Lecture notes in statistics. Springer, New York, NY, second edition edition, 2025.
- [13] Giorgia Pase. *Towards parametric estimation and efficient hemodynamics simulations of cardiac valves*:. PhD thesis, University of Groningen, September 2025.
- [14] Ahmed Attia, Alen Alexanderian, and Arvind K Saibaba. Goal-oriented optimal design of experiments for large-scale bayesian linear inverse problems. *Inverse Problems*, 34(9):095009, 2018.
- [15] Alen Alexanderian. Optimal experimental design for infinite-dimensional Bayesian inverse problems governed by PDEs: a review. *Inverse Problems*, 37(4):043001, April 2021.
- [16] Abhijit Chowdhary, Shady E. Ahmed, and Ahmed Attia. PyOED: An Extensible Suite for Data Assimilation and Model-Constrained Optimal Design of Experiments. *ACM Transactions on Mathematical Software*, 50(2):1–22, June 2024.
- [17] Jeremías Garay, David Nolte, Miriam Löcke, and Cristóbal Bertoglio. Parameter estimation in fluid flow models from aliased velocity measurements. *Inverse Problems*, 38(9):095002, August 2022.
- [18] Ahmed Attia, Sven Leyffer, and Todd S Munson. Stochastic learning approach for binary optimization: Application to bayesian optimal design of experiments. *SIAM Journal on Scientific Computing*, 44(2):B395–B427, 2022.
- [19] Ahmed Attia. Probabilistic approach to black-box binary optimization with budget constraints: Application to sensor placement. *arXiv preprint arXiv:2406.05830*, 2024.
- [20] Ahmed Attia and Emil Constantinescu. Optimal experimental design for inverse problems in the presence of observation correlations. *SIAM Journal on Scientific Computing*, 44(4):A2808–A2842, 2022.
- [21] SM Ermakov et al. Mathematical theory of experimental design. *M. Science*, 1983.

- [22] Alen Alexanderian, Hugo Díaz, Vishwas Rao, and Arvind K. Saibaba. Optimal sensor placement under model uncertainty in the weak-constraint 4D-Var framework, May 2025. arXiv:2502.00150 [math].

A Numerical solution method of the flow model

Here we detail the algorithm used to solve the incompressible Navier-Stokes equation with Windkessel boundary conditions for the forward problem.

Algorithm 3 Fractional step algorithm with a modified semi-implicit Windkessel model coupling

Given the initial conditions $\mathbf{u}^0 = \mathbf{u}(0) \in V_{\Gamma_w, h}$ and $\pi_1^0, \dots, \pi_N^0 \in \mathbb{R}$, perform for $j > 0$, with $t^j = j\tau$:

1. Viscous Step: Find the tentative velocity $\tilde{\mathbf{u}}^n \in V_{\Gamma_w, h}$ such that:

$$\left\{ \begin{array}{l} \tilde{\mathbf{u}}^j|_{\Gamma_{in}} = \mathbf{u}_{inlet}(t^j) \\ \frac{\tau}{\rho}(\tilde{\mathbf{u}}^j, \mathbf{v})_{\Omega_h} + \rho(\mathbf{u}^{j-1} \cdot \nabla \tilde{\mathbf{u}}^j, \mathbf{v})_{\Omega_h} + \frac{\rho}{2}((\nabla \cdot \mathbf{u}^{j-1})\tilde{\mathbf{u}}^j, \mathbf{v})_{\Omega_h} + (\delta \mathbf{u}^{j-1} \cdot \nabla \tilde{\mathbf{u}}^j, \mathbf{u}^{j-1} \cdot \nabla \mathbf{v})_{\Omega_h} \\ + 2\mu(\epsilon(\tilde{\mathbf{u}}^j), \epsilon(\mathbf{v}))_{\Omega_h} + \sum_{\ell=1}^K \frac{\rho}{2}|\mathbf{u}^{j-1} \cdot \mathbf{n}|_-(\tilde{\mathbf{u}}^j, \mathbf{v})_{\Gamma_\ell} = \frac{\tau}{\rho}(\mathbf{u}^{j-1}, \mathbf{v})_{\Omega_h} \end{array} \right. \quad (20)$$

for all $\mathbf{v} \in V_{\Gamma_{in} \cup \Gamma_w, h}$, and $|x|_-$ denoting the negative part of x .

2. Projection-Windkessel Step: Compute $\tilde{Q}^j = \int_{\Gamma_\ell} \tilde{\mathbf{u}}^j \cdot \mathbf{j}$. Find $p^j \in Q_h$ such that:

$$\frac{\tau}{\rho}(\nabla p^j, \nabla q)_{\Omega_h} + \sum_{\ell=1}^K \frac{\overline{p^j}_{\Gamma_\ell} \overline{q}_{\Gamma_\ell}}{\gamma_\ell} + \epsilon \sum_{\ell=1}^K (\mathcal{T}(\nabla p^j), \mathcal{T}(\nabla q))_{\Gamma_\ell} = \sum_{\ell=1}^K \left(\tilde{Q}^j + \frac{\alpha_\ell \pi_\ell^{j-1}}{\gamma_\ell} \right) \overline{q}_{\Gamma_\ell} - (\nabla \cdot \tilde{\mathbf{u}}^j, q)_{\Omega_h}, \quad (21)$$

for all $q \in Q_h$ and with $\overline{(\cdot)}_{\Gamma_\ell} = \frac{1}{\text{Area}(\Gamma_\ell)} \int_{\Gamma_\ell} (\cdot) ds$ and $\mathcal{T}(\mathbf{f}) = \mathbf{f} - (\mathbf{f} \cdot \mathbf{j})\mathbf{j}$.

3. Velocity correction Step: Find $\mathbf{u}^j \in [L^2(\Omega_h)]^3$ such that:

$$(\mathbf{u}^j, \mathbf{v})_{\Omega_h} = (\tilde{\mathbf{u}}^j - \frac{\tau}{\rho} \nabla p^j, \mathbf{v})_{\Omega_h}$$

for all $\mathbf{v} \in [L^2(\Omega_h)]^3$

4. Update-Windkessel Step: Set $P_\ell^j = \overline{p^j}_{\Gamma_\ell}$ and compute $\pi_\ell^j \in \mathbb{R}$ as:

$$\pi_\ell^j = \left(\alpha_\ell - \frac{\alpha_\ell \beta_\ell}{\gamma_\ell} \right) \pi_\ell^{j-1} + \frac{\beta_\ell}{\gamma_\ell} P_\ell^j, \quad \ell = 1, \dots, K$$

B The Reduced-Order Unscented Kalman Filter

The ROUKF algorithm is as follows:

Let us first consider the notation $\mathbf{Z}_{(*)}$ as the matrix with the column-wise collection of vectors $\mathbf{Z}_{(1)}, \mathbf{Z}_{(2)}, \dots$.

Define the *canonical sigma-points* $\mathbf{I}_{(1)}, \dots, \mathbf{I}_{(2p)} \in \mathbb{R}^p$ such that

$$\mathbf{I}_{(j)} = \begin{cases} \sqrt{p}\mathbf{e}_j, & \text{for } 1 \leq j \leq p \\ -\sqrt{p}\mathbf{e}_{j-p}, & \text{for } p+1 \leq j \leq 2p \end{cases} \quad (22)$$

where the vectors \mathbf{e}_i form the canonical base of \mathbb{R}^p . Moreover, define the weight $\alpha = \frac{1}{2p}$.

We denote by $\hat{\mathbf{X}}_-^n, \hat{\mathbf{X}}_+^n \in \mathbb{R}^r$ a priori (model prediction) and a posteriori (corrected by observations) estimates of the true state $\mathbf{X}^n \in \mathbb{R}^r$. In our PDEs, this consists of the velocity field $\mathbf{X}^n = \mathcal{A}^n(\boldsymbol{\theta})$.

For given values of the initial condition $\hat{\mathbf{X}}_+^0 = \mathbf{X}_0 \in \mathbb{R}^r$, the initial expected value of the parameters $\hat{\boldsymbol{\theta}}_+^0 = \boldsymbol{\theta}_0 \in \mathbb{R}^p$ and its covariance matrix \mathbf{P}_0 , perform

- **Initialization:** initialize the sensitivities as

$$\mathbf{L}_\theta^0 = \sqrt{\mathbf{P}_0} \text{ (Cholesky factor)}, \quad \mathbf{L}_X^0 = \mathbf{0} \in \mathbb{R}^{r \times p}, \quad \mathbf{U}^0 = \mathbf{P}_\alpha \equiv \alpha \mathbf{I}_{(*)}(\mathbf{I}_{(*)})^T \quad (23a)$$

Then, for $k = 1, \dots, N_T$:

- **Sampling:** generate $2p$ particles from the current state and parameter estimates, i.e. for $i = 1, \dots, 2p$:

$$\begin{cases} \hat{\mathbf{X}}_{(i)}^{k-1} = \hat{\mathbf{X}}_+^{k-1} + \mathbf{L}_X^{k-1}(\mathbf{C}^{k-1})^T \mathbf{I}_{(i)}, \\ 1 \leq i \leq p+1 \\ \hat{\boldsymbol{\theta}}_{(i)}^{k-1} = \hat{\boldsymbol{\theta}}_+^{k-1} + \mathbf{L}_\theta^{k-1}(\mathbf{C}^{k-1})^T \mathbf{I}_{(i)} \end{cases} \quad (23b)$$

with \mathbf{C}^{k-1} the lower Cholesky factor of $(\mathbf{U}^{k-1})^{-1}$.

- **Prediction:** propagate each particle with the forward model and compute an a priori state prediction:

$$\begin{cases} \hat{\mathbf{X}}_{(i)}^k = \mathcal{A}^k(\hat{\mathbf{X}}_{(i)}^{k-1}, \hat{\boldsymbol{\theta}}_{(i)}^{k-1}), \quad \hat{\boldsymbol{\theta}}_{(i)}^k = \hat{\boldsymbol{\theta}}_{(i)}^{k-1}, \quad i = 1, \dots, 2p \\ \hat{\mathbf{X}}_-^k = E_\alpha(\hat{\mathbf{X}}_{(*)}^k) \equiv \alpha \sum_{i=1}^{2p} \hat{\mathbf{X}}_{(i)}^k \\ \hat{\boldsymbol{\theta}}_-^k = E_\alpha(\hat{\boldsymbol{\theta}}_{(*)}^k) \end{cases} \quad (23c)$$

- **Innovation computation:** for each particle j , compute the innovation $\boldsymbol{\Gamma}_{(j)}^k$: First, compute

$$\tilde{\boldsymbol{\Gamma}}_{(j)}^k = \begin{bmatrix} \Re(\mathbf{Y}^k) - \Re(\mathcal{H}_{\mathcal{F}}(\mathcal{H}(\mathcal{A}^k(\boldsymbol{\theta}_{(j)})))) \\ \Im(\mathbf{Y}^k) - \Im(\mathcal{H}_{\mathcal{F}}(\mathcal{H}(\mathcal{A}^k(\boldsymbol{\theta}_{(j)})))) \end{bmatrix} \in \mathbb{R}^{2 \times N_x \times N_y \times N_z} \quad (23d)$$

and then construct the innovation by excluding all zero values and mapping the matrix to a vector of equivalent dimension, leading to a vector $\boldsymbol{\Gamma}_{(j)}^k \in \mathbb{R}^{2N_S}$ where N_S is the number of sampled frequencies.

- **Correction:** compute a posteriori estimates based on measurements for state and parameters, using the i -th particle innovation $\boldsymbol{\Gamma}_{(i)}^k$:

$$\left\{ \begin{array}{l} \mathbf{L}_X^k = \alpha \hat{\mathbf{X}}_{(*)}^k (\mathbf{I}_{(*)})^T \\ \mathbf{L}_\theta^k = \alpha \hat{\boldsymbol{\theta}}_{(*)}^k (\mathbf{I}_{(*)})^T \\ \mathbf{L}_\Gamma^k = \alpha \boldsymbol{\Gamma}_{(*)}^k (\mathbf{I}_{(*)})^T \\ \mathbf{U}^k = \mathbf{P}_\alpha + (\mathbf{L}_\Gamma^k)^T \mathbf{W}^{-1} \mathbf{L}_\Gamma^k \\ \hat{\mathbf{X}}_+^k = \hat{\mathbf{X}}_-^k - \mathbf{L}_X^k (\mathbf{U}^k)^{-1} (\mathbf{L}_\Gamma^k)^T \mathbf{W}^{-1} E_\alpha(\boldsymbol{\Gamma}_{(*)}^k) \\ \hat{\boldsymbol{\theta}}_+^k = \hat{\boldsymbol{\theta}}_-^k - \mathbf{L}_\theta^k (\mathbf{U}^k)^{-1} (\mathbf{L}_\Gamma^k)^T \mathbf{W}^{-1} E_\alpha(\boldsymbol{\Gamma}_{(*)}^k) \\ \mathbf{P}_\theta^k = \mathbf{L}_\theta^k (\mathbf{U}^k)^{-1} (\mathbf{L}_\theta^k)^T \end{array} \right. \quad (23e)$$

with $\mathbf{W} = \sigma_y^2 \mathbb{I}$.